

Integrating petrophysical, geological and geomechanical modelling to assess stress states, overpressure development and compartmentalisation adjacent to a salt wall, gulf of Mexico

J. Obradors-Prats^{a,c}, E.E. Calderon Medina^{b,*}, S.J. Jones^b, M. Rouainia^a, A.C. Aplin^b, A.J.L. Crook^c

^a School of Engineering, Newcastle University, Newcastle Upon Tyne, NE1 7RU, UK

^b Department of Earth Sciences, Durham University, Durham, DH1 3LE, UK

^c Three Cliffs Geomechanical Analysis Ltd, Swansea, Wales

ARTICLE INFO

Keywords:

Overpressure
Geomechanical modelling
Log analysis
Salt tectonics
Pressure compartmentalisation
Seismic interpretation
Finite element
Gulf of Mexico

ABSTRACT

Multi-well pressure data from the Magnolia Field, located on a flank of the salt-bounded Titan passive mini-basin in the Garden Banks area of the continental slope of the Gulf of Mexico, indicate remarkably high overpressures that vary, at similar depths, by up to 10 MPa between sand bodies 1 km apart. In the present paper, we integrate geological and geophysical analysis with 2D forward hydro-mechanical evolutionary modelling to assess the contribution of both disequilibrium compaction and diapir-related tectonic loading to the observed overpressure and to understand controls on pressure compartmentalisation. The 2D finite element evolutionary model captured the sedimentation of isolated sand channels bounded by mud-dominated sediments close to a rising salt wall which led to tectonic loading on sediments. Comparison of results from the 2D and 1D models shows that disequilibrium compaction can explain most of the overpressure as a result of very rapid deposition of mainly mud-rich, low permeability sediments; tectonic loading contributes around 7% of the observed overpressure. The models also show that linked to the high sedimentation rates, small variations in the permeability and connectivity of the mud-rich sections that bound the channel sands result in highly compartmentalised pressure distributions in adjacent sand bodies.

1. Introduction

Overpressure, i.e., pore fluid pressures in excess of the hydrostatic gradient, exerts a major influence on a range of major geological processes including subsidence, slope failure, faulting and folding (e.g., Dickinson, 1953; Hubbert and Rubey, 1959; Dugan and Flemings, 2000; Ostermeier et al., 2000; Saffer and Tobin, 2011; Berndt et al., 2012). From a geoengineering perspective, a quantitative understanding of overpressure also underpins the safe design of wellbore drilling operations, as well as the injection rates and maximum volume of geological CO₂ storage without compromising the integrity of the overburden.

Overpressure in sedimentary basins can develop via several mechanisms, often in combination, including disequilibrium compaction (Swarbrick, 2012), tectonic deformation (Luo et al., 2007; Couzens-Schultz and Azbel, 2014), lateral transfer (Yardley and Swarbrick, 2000; Heaton et al., 2020), diagenesis (Lahann and Swarbrick, 2011; Nguyen

et al., 2016), hydrocarbon generation and hydrocarbon-related buoyant pressure (Liu et al., 2019; Li et al., 2021), and aquathermal expansion (Osborne and Swarbrick, 1997; Luo and Vasseur, 1992).

In many cases, pore pressure must be estimated indirectly, either because the information is required before drilling is undertaken and/or because it cannot be directly measured, especially for lithologies with low permeabilities that would require unfeasibly long measurement times. Estimates and predictions can be made using a range of methods including well log analysis, (Zhang, 2011; Azadpoura et al., 2015; Gouly and Sargent, 2016), seismic interval stacked velocities (Sayers et al., 2002; Brahma et al., 2013; Bahmaei and Hosseini, 2020), and numerical basin modelling (Flemings and Lupa, 2004; Broichhausen et al., 2005; Hantschel and Kauerauf, 2009; Neumaier et al., 2014).

Forward geomechanical modelling over geological time scales is a type of basin modelling that relies on physical principles to capture the evolution of the basin due to the constitutive response of the geological

* Corresponding author.

E-mail address: erika.e.calderon-medina@durham.ac.uk (E.E. Calderon Medina).

<https://doi.org/10.1016/j.marpetgeo.2023.106352>

Received 6 December 2022; Received in revised form 8 May 2023; Accepted 1 June 2023

Available online 2 June 2023

0264-8172/© 2023 The Authors. Published by Elsevier Ltd. This is an open access article under the CC BY license (<http://creativecommons.org/licenses/by/4.0/>).

materials to the imposed boundary conditions. It can simulate the evolution of geological structures, stress, strain, and pore pressure states during basin history, from a target paleo time to present day. This technique has been used to investigate the controls on the development of geological structures (Crook et al., 2006; Vidal-Royo et al., 2011; Albertz and Lingrey, 2012; Thornton and Crook, 2014; Roberts et al., 2015; Ruh, 2017), and the impact of the evolutionary deformation structures in the stress-strain and pore pressure fields (Albertz and Sanz, 2012; Smart et al., 2012; Obradors-Prats et al., 2016, 2017b). It also facilitates a better understanding of stress fields and pore pressures in systems influenced by salt tectonics (Nikolinakou et al., 2014, 2018; Heidari et al., 2016, 2021; Luo et al., 2017; Lovely et al., 2018).

In this paper we build fully coupled hydro-mechanical forward models to understand the development and distribution of overpressure

in the Magnolia Field. This field is located on a flank of the salt-bounded Titan mini-basin, in the Garden Banks area of the continental slope of the Gulf of Mexico (Fig. 1a). Overpressure in this region is complex; multi-well pressure data indicate remarkably high overpressures that vary significantly between spatially close sand bodies at similar depths (Sathar and Jones, 2016).

A 3D seismic cube, log-based interpretation, core analysis and reservoir characterisation were used to derive the present-day structural configuration and build a detailed sedimentary model. Petrophysical analysis using wireline log data is used to assess mechanisms contributing to overpressure formation in the Magnolia Field. This information is then used to build the coupled geomechanical model, including a geomechanical restoration that informs the depositional inputs for the forward model in a qualitative manner. The model captures the

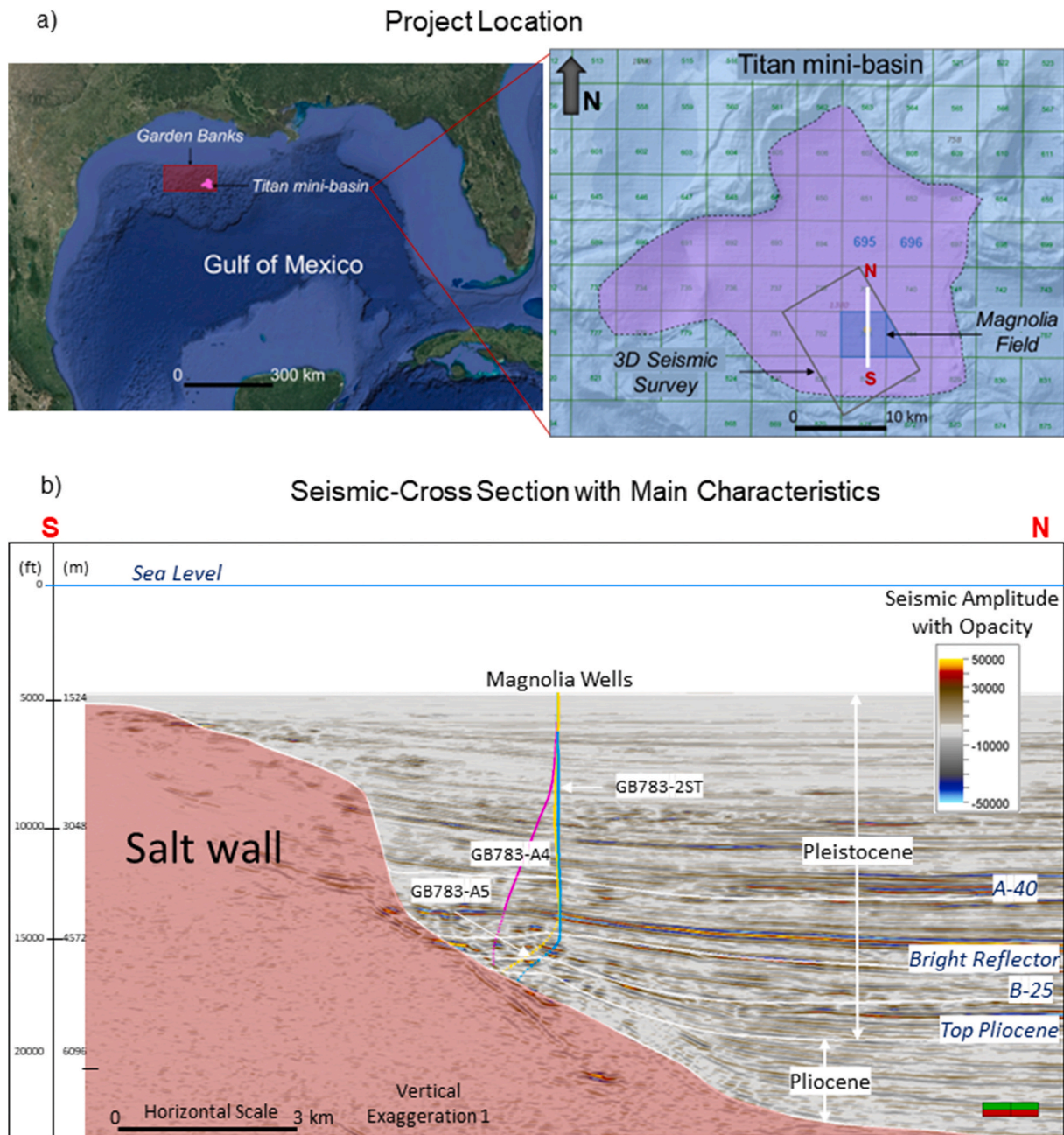


Fig. 1. (a) Location of the Titan min-basin, Magnolia Field, seismic cubes, and location of the N–S seismic cross-section (Source BOEM, 2021). (b) S–N seismic cross-section used in the geomechanical models showing wells GB783-A4, GB783-A5 and GB783-2ST, the top of the reservoirs A-40, B-25, a bright reflector, top Pliocene and top of the salt wall.

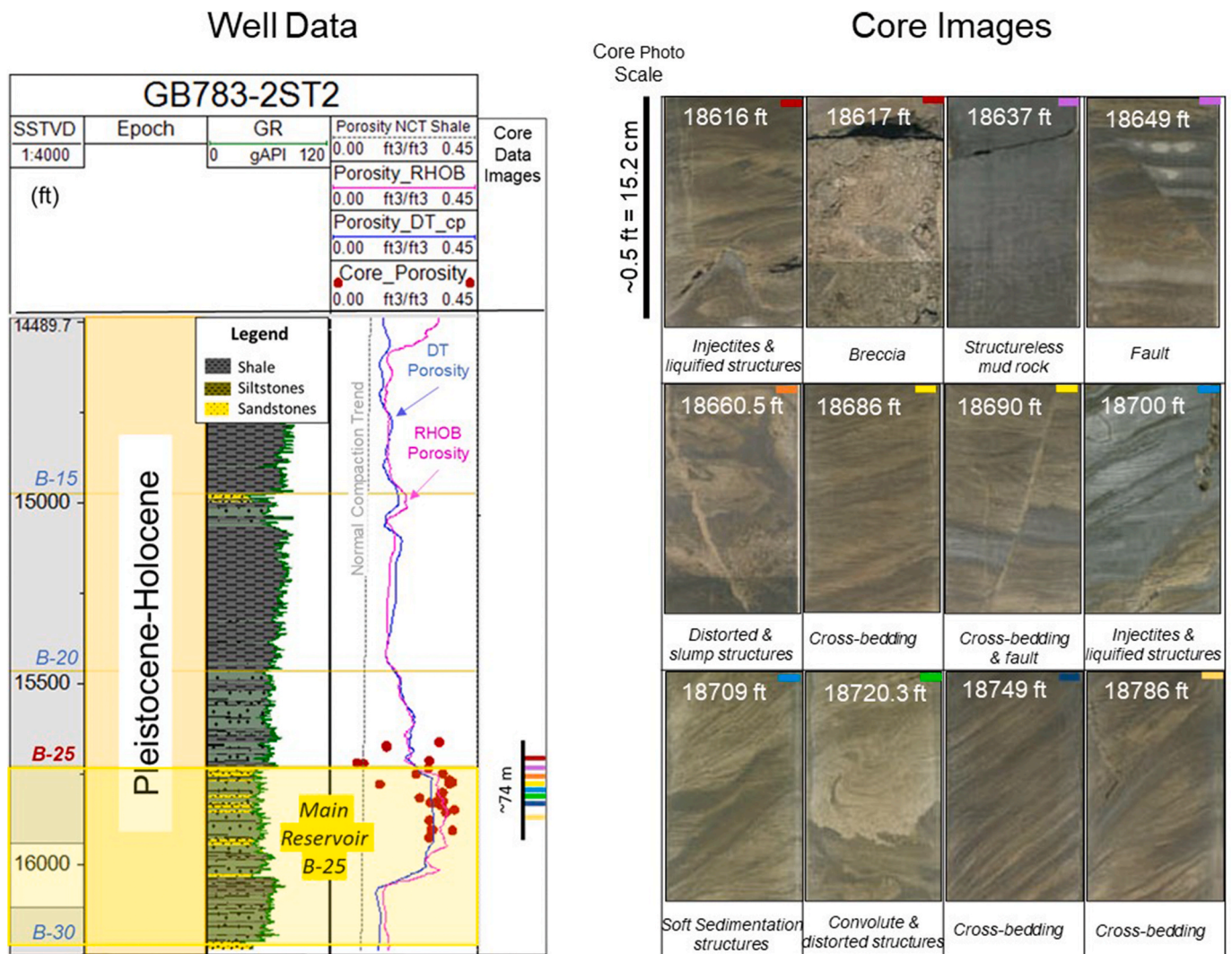


Fig. 2. Well log and core images highlighting the sedimentary structures, well GB783-2ST2 (Source: CoreLab, 2003).

structural evolution of the sediment formations as well as the adjacent rising salt wall and is calibrated to predict a geometry consistent with the seismic interpretation. Overpressure generation mechanisms captured by the models are disequilibrium compaction, salt-induced tectonic strain, and lateral transfer. Porosity-permeability curves used in the geomechanical models are calibrated to predict an overpressure magnitude consistent with measurements for the target reservoir B-25 (Fig. 1b).

Finally, the modelling results are used in conjunction with the petrophysical analysis to first quantify the relative contribution of the different mechanisms in generating the observed overpressure and to then understand potential factors contributing to overpressure compartmentalisation in the Magnolia Field sand reservoirs.

2. Geology

For this study, a set of well logs, 3D seismic cubes in time and depth, check shots, pressure tests as well as core and drilling reports were used (Table 1). Well correlation, seismic and lithofacies interpretation, pressure analysis and definition of static models were performed with Petrel software (version 2022). Techlog software (version 2018) was used for petrophysical interpretation.

Table 1

Summary of the data used in this study.

Data	Number of Wells
Wells and deviation trajectory	25
Drilling reports	8
Logs GR (2400 m TVDSS - TD), DT (~2850 m TVDSS- TD) and resistivity (~3760 m TVDSS - TD)	2
Logs GR, DT, resistivity, RHOB and NPHI (reservoirs)	22
Check shots (include data from other fields in the area)	30
3D seismic cubes (time and depth) with an area of 130 km ²	1
Pressure data (Reservoirs B-25) + (other reservoirs)	12 + 5
Core data report	1

2.1. Geological setting

The Magnolia Field spans blocks 783 and 784 within the Titan mini-basin in the Garden Banks area of the continental slope in the Gulf of Mexico (Fig. 1a). This field is under a water column of 1424 m (4674 ft) (Stomp et al., 2004; Eaton et al., 2005; Colwart et al., 2007). The Titan mini-basin depocenter has a thickness of approximately 11 km of Upper Miocene to Pleistocene sediments deposited on top of the allochthonous salt sourced from the Louann Jurassic salt formation (Fig. 1b) (Weissenburger and Borbas, 2004; Sathar and Jones, 2016).

In the Magnolia Field the sediments are mud-dominated, Pliocene to Pleistocene in age and up to 5 km thick (Fig. 1b). Most of the lithofacies within the reservoir section correspond to deepwater channel systems which contain silt- and sand-rich sections.

Twenty-five wells were drilled in this field during exploration and development to a maximum depth of 5200 m (17,060 ft) below sea level, targeting nineteen fine sand and siltstone intervals for oil and gas production. Reservoir B-25 was the most prolific reservoir with an expected recovery factor of sixty percent (Procyk et al., 2007).

Hydrocarbon indicators such as flat spots were not identified in any of the reservoirs during seismic interpretation, but pressure data show different oil and gas water contacts in each reservoir. Bright reflectors are present at different depths (as seen in Fig. 1b) although they are not continuous.

An indication of active salt tectonics during the deposition of Pliocene and Pleistocene sediments is observed in the thickness variation and the angle of the reflectors. Near the salt wall, seismic reflectors are almost vertical, and the thickness is reduced in comparison to the sediments towards the centre of the Titan mini-basin where the reflectors are approximately horizontal with greater thickness (Fig. 1b).

Interpretation of the 3D seismic survey was performed in time and depth to derive the structural configuration of the area. Seismic attributes such as structural smoothing, variance, chaos, sweetness, and RMS were created to facilitate the interpretation. Due to the quality and chaotic nature of the seismic data the interpretation close to the salt wall could differ from other interpretations (Fig. 1b).

2.2. Sedimentary column analysis

The overburden was characterised with well logs and reports from two wells, GB783-1 and GB783-A8 with data available from 2777 m (9000 ft) and 2386 m (7820 ft) TVDSS respectively (Fig. 3a and b and Fig. 5a). The mud-dominated sediments consist of thin intercalations of sandstone, siltstone, and shale (mudstone).

The Pleistocene B-25 reservoir (focus of this study) has a thickness variation between 67 m (220 ft) and 265 m (870 ft), with net to gross (NTG) ratios ranging from 0.13 to 0.92 (fraction). Potential vertical and horizontal barriers to fluid flow have been interpreted in ~74 m (242.85 ft) of core images from Well GB783-2ST2, located approximately 1433 m (4700 ft) towards the north from the main diapir wall (Fig. 3a). These include features such as high angle crossbedding, fractures, small scale faults and lithological heterogeneity (Fig. 2).

Core measurements indicate porosity values between 0.04 and 0.37 (fraction) and permeabilities between 0.001 and 487 mD. No features indicative of clay mineral or quartz diagenesis were identified on photos and thin sections of the B-25 and B-20 reservoirs.

A field scale analysis using pressure tests, seismic and well log data was performed, and the results show both, high compartmentalisation and hydraulic connection between different wells.

Fig. 3a shows a structural map of the B-25 reservoir top and salt wall surfaces displaying the location of the thirteen wells where B-25 pressure data was available. A line from points A to A' defines a seismic section shown in Fig. 3b intersecting six of the seven wells which are hydraulically connected. Isolated reflectors can be observed within the seismic data, but their connectivity could not be fully established due to insufficient seismic resolution, which is ~20 m (~65 ft equivalent to 16 ms). In Fig. 3c the corresponding well correlation with GR, lithologies and sonic logs is provided. An interpretation of the thin sand-silt intercalation of the B-25 reservoir is also presented. However, there is no clear indication of connectivity between these thin intercalations. No production data were available to calibrate the volume, size, or shape of each reservoir in this study.

2.3. Measured fluid pressures

MDT pore pressures in these wells are up to 76 MPa (11,000 psi) at

approximately 5000 m TVDSS (16,400 ft), at which depth temperatures are between 60 and 70 °C (Sathar and Jones, 2016). Due to the low temperatures and rapid sedimentation of mud-dominated lithologies, an initial hypothesis is that most of the overpressure has been generated by disequilibrium compaction (Ostermeier et al., 2000, 2001; Sathar and Jones, 2016). However, other overpressure generation mechanisms cannot be excluded, such as the impact of salt tectonics and lateral transfer along potentially laterally extensive, dipping, permeable horizons (e.g., pressure transfer from deep sediments located in the mini-basin depocenter towards the Magnolia Field, Fig. 1a).

From the pressure-depth plot, it is observed that all nineteen reservoirs (i.e., A-63, A-80, A-85, A-90, B-10, B-12, B-13, B-15, B-17, B-20, B-25, B-30, C-30, C-40, C-50, C-60, C-70, D-10 and Miocene) in all wells are overpressured, with measurements indicating a high degree of vertical and horizontal fluid compartmentalisation (Fig. 4a).

Reservoir B-25 was chosen for a detailed analysis due to the number of tests available. Gas, oil, and water pressure gradients were identified (Fig. 4b). Hydraulic connectivity was interpreted in the GB784-A6, GB784-A8, GB783-1ST1BP1, GB783-1, GB784-A7, GB783-A9 and GB783-3 wells (Fig. 3). On the other hand, high pressure compartmentalisation was identified in the GB783-A4, GB783-A5, GB783-2ST, GB783-2 and GB783-3ST wells. It is noted that these wells, which have larger overpressure values than the hydraulically connected wells, are located closer to the salt wall. For example, well GB783-A4, which is the closest well to the salt wall (Fig. 3a), also has the highest pore pressure ~79 MPa (11,500 psi), which is approximately 28 MPa (4000 psi) above the hydrostatic pressure (Fig. 4b).

3. Log-based assessment of pore pressure

As porosity loss by mechanical compaction is driven by effective stress, the analysis of porosity (or porosity proxies such as transit time and density) as a function of depth allows estimates to be made of effective stress and thus pore pressure. Overpressure is inferred when sediments have porosities that are higher than those consistent with an effective stress where pore pressures are hydrostatic, defined as a “normal compaction trend” (NCT). In this study, it is reasonable to assume that mechanical compaction is the main cause of the overpressure because temperatures are below 70 °C and non-mechanical (chemical) compaction, related to clay mineral diagenesis or quartz cementation, is very unlikely to be important.

The definition of an NCT or, more broadly, a relationship between porosity and effective stress, is not straightforward in this study because there are neither porosity nor porosity-related log data (transit time; density) in the top 1600 m (5185 ft) of the sediment column and drilling data suggest that overpressure occurs at depths greater than 300 m (972 ft). NCTs have therefore been defined based on sonic and density logs which had been developed for mechanically compacted sediments from the Gulf of Mexico.

Normal compaction trends based on sonic and density logs were generated using Wyllie et al. (1956) and Athy's (1930) equations (1) and (2):

$$\Delta t_{NC} = \Delta t_{ma} + (\Delta t_{ml} - \Delta t_{ma}) * e^{-c*Z} \quad 1$$

$$= \rho_{ma} + (\rho_{ml} - \rho_{ma}) * e^{-c*Z} \quad 2$$

where Δt_{NC} is the transit time of the normal compaction, Δt_{ma} is the matrix transit time (67 μ s/ft), Δt_{ml} is the mudline transit time (seabed) (188 μ s/ft), z is the depth below sea level (m), c is the compaction coefficient (0.0005 m^{-1}) after Hansen (1996) and Tingay et al. (2009), ρ_{NC} is the density of the normal compaction, ρ_{ma} is the matrix density (2.67 gr/cm^3) and ρ_{ml} is the density at the mudline (1.73 gr/cm^3).

Porosities were estimated from the sonic and density logs using equations (3) and (4):

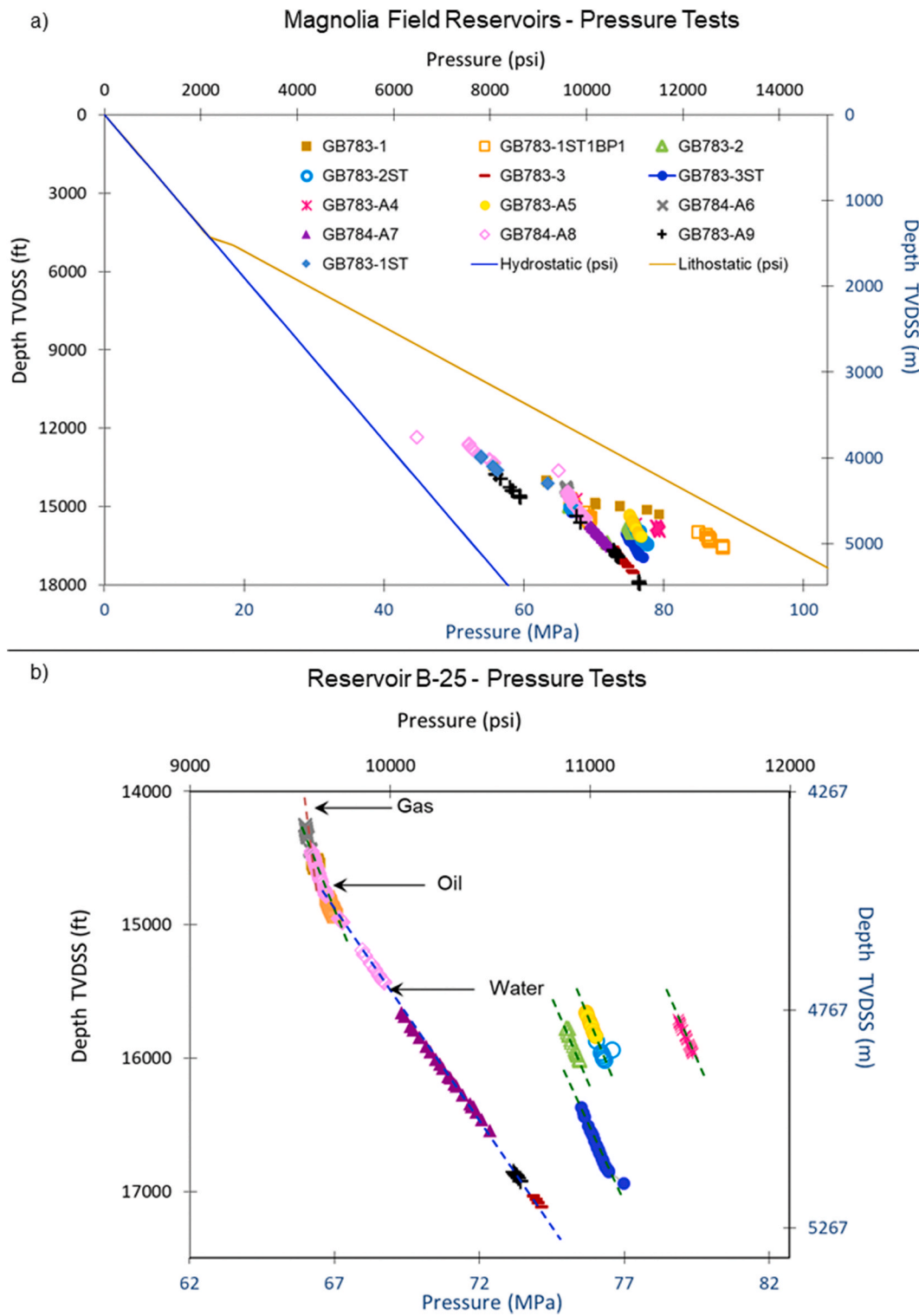


Fig. 4. a) Modular dynamic formation tester (MDT) data of thirteen wells and seventeen reservoirs of the Magnolia Field. Hydrostatic pressure gradient was estimated to be 0.00105 MPa/m (0.465 psi/ft) and the lithostatic pressure gradient 0.0226 MPa/m (1 psi/ft). b) pressure plots of tests performed in twelve wells, reservoir B-25, Magnolia Field. Red, green, and blue discontinuous lines indicate gas, oil, and water pressure gradients, respectively.

$$\phi_{DTep} = \frac{\Delta t - \Delta t_{ma}}{\Delta t_f - \Delta t_{ma}} \cdot C_p$$

$$\phi_{density} = \frac{\rho_{ma} - \rho_b}{\rho_{ma} - \rho_f}$$

where ϕ_{DTep} is the corrected porosity from sonic log, C_p is the correction

factor considered to be 1.8 after Raymer et al. (1980); Issler (1992); Hart et al. (1995); Schlumberger (1989) and Tingay et al. (2009), Δt_{ma} is the matrix transit time (67 μ s/ft), Δt is the measured transit time (us/ft), Δt_f is the fluid transit time (188 μ s/ft), $\phi_{density}$ is the porosity from density log, ρ_{ma} is the matrix density (2.67g/cm³), ρ_b is the bulk density measured (g/cm³) and ρ_f is the fluid density (1.03 g/cm³).

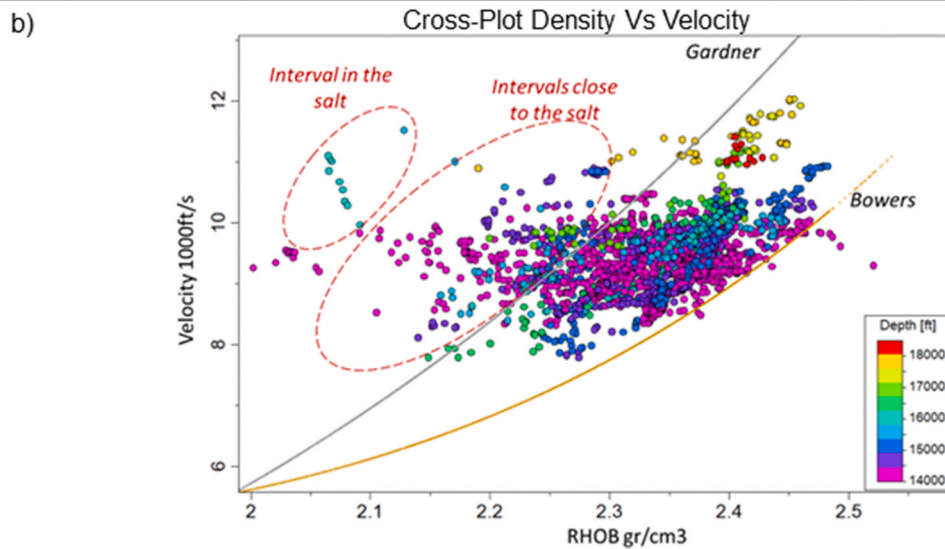
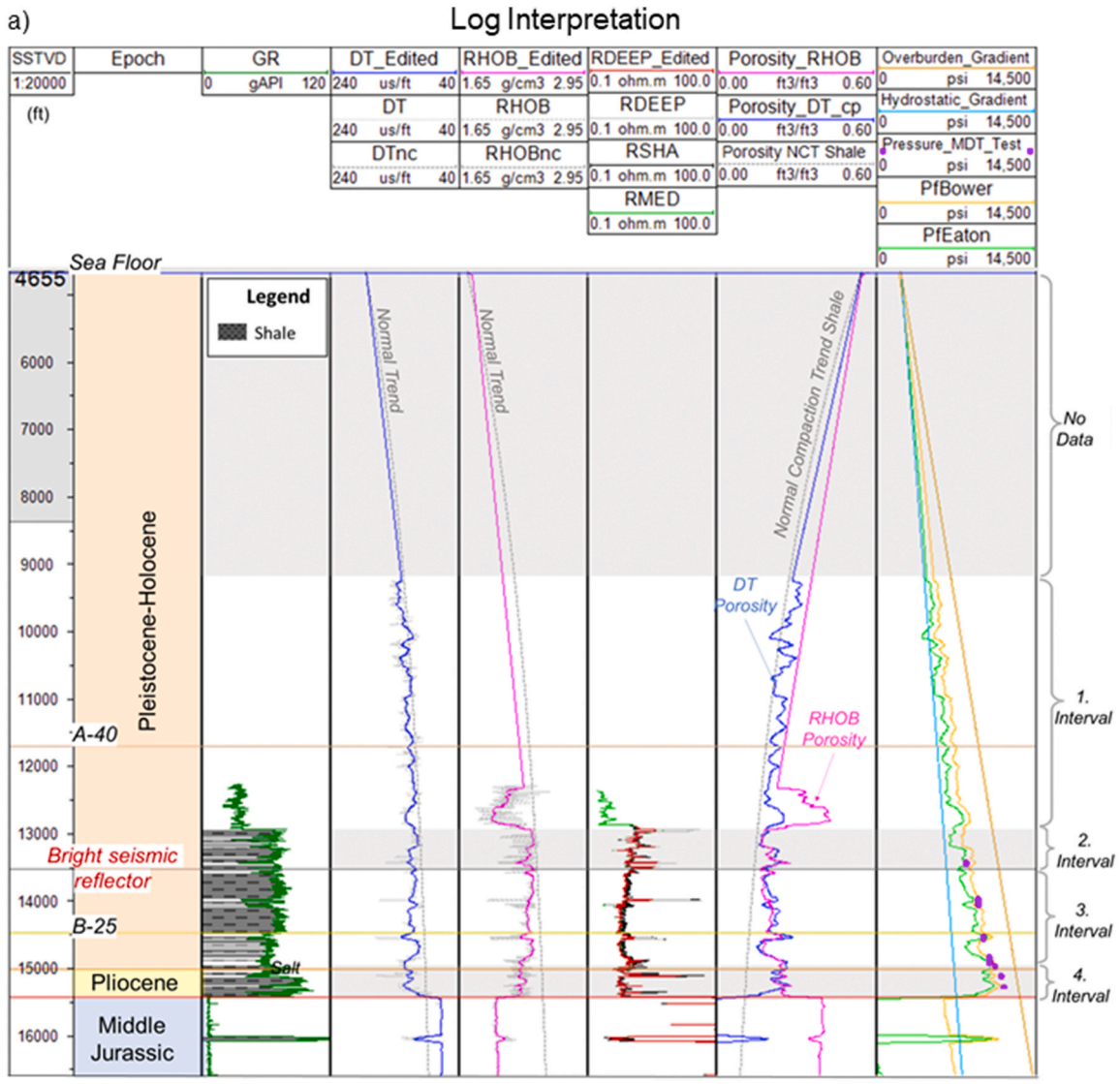


Fig. 5. a) Pore pressure interpretation based on well logs data, Well GB783-1. Normal compaction trends for transit time and density are from equations (1) and (2). Porosities were calculated from equations (3) and (4). Pore fluid pressure trends are from equations (5) and (6). b) density-velocity cross-plot of eight wells with a filter on shale and depth >3700 m 12,000 ft TVDSS).

Pore fluid pressure was estimated from sonic logs using relationships developed for mechanically compacted Gulf of Mexico mudstones by Eaton (1975) (equation (5)) and Bowers (1995) (equation (6)).

$$P_f = \sigma_L - (\sigma_L - \sigma_{Hy}) \left(\frac{\Delta t_{NC}}{\Delta t} \right)^x \quad 5$$

$$P_f = \sigma_L - \left(10^6 * \frac{\frac{1}{\Delta t} - \frac{1}{\Delta t_{ml}}}{a} \right)^{\frac{1}{b}} \quad 6$$

Where P_f is the pore pressure fluid, σ_{Hy} is the hydrostatic pore pressure, σ_L is equal to the lithostatic stress/overburden, Δt_{NC} is the normal compaction transit time for hydrostatically pressured sediment (us/ft), Δt is the transit time from sonic log (us/ft), Δt_{ma} is the matrix transit time (67 us/ft), Δt_{ml} is the transit time at sea floor (188 us/ft) and x is the exponent 3 (Eaton, 1975).

Results from the well log analysis are presented in Fig. 5a. The lack of log data precludes any analysis shallower than 2777 m TVDSS (~9000 ft), but the log data at greater depths are consistent with increasing overpressure with increasing depth.

There is a fairly constant density and a slight increase in transit time at depths greater than 3953 m TVDSS (12,970 ft). A constant density or transit time with increasing depth indicates a constant effective stress, which occurs where the rate of additional pore pressure is due to sedimentation-related loading being much faster than the rate at which pore pressure can decrease due to fluid flow. This occurs at the so-called “fluid isolation depth” (Swarbrick, 2012).

An increase in transit time and decrease in density with depth below 4127 m TVDSS (13,543 ft), which correlates to one of the bright reflectors observed on the seismic data, suggests that in well GB783-1, this section reached the fluid isolation depth at a slightly shallower depth than in the section immediately above (Fig. 1b and 5b).

Pore pressures measured in the upper parts of the more sand-rich reservoir section are similar to those inferred from the Bowers (1995) log analysis of the overlying mud-rich section (Fig. 5a). This implies that the pore pressures can be largely explained as being generated by disequilibrium compaction, which is expected in a sedimentary system dominated by the rapid deposition of low permeability mudstones, and which has not been subjected to chemical diagenesis.

The fit is not as good at the base of the sand-rich section (reservoir B-25) below a very sharp ramp of pore pressure 4572 m TVDSS (15,000 ft), suggesting that overpressure mechanisms in addition to disequilibrium compaction may be operating. These could include tectonic stress and lateral transfer (Yardley and Swarbrick, 2000), the analysis of which requires a more sophisticated approach using 2D hydro-mechanical modelling.

Density-velocity cross-plots are particularly useful to identify situations where unloading has occurred, because for a given decrease in effective stress, the relative decrease in velocity is much greater than that of density (Bowers and Katsube, 2002).

Both Bowers (2001) and Gardner (1974) developed density-velocity relationships for mudstones from the Gulf of Mexico and Gulf Coast where disequilibrium compaction was identified to be the main overpressure generating mechanism (equations (7) and (8)).

$$V = 4790 + 2953 * (\rho - 1.3)^{3.57} \quad 7$$

$$V = \left(\frac{\rho}{0.23} \right)^4 \quad 8$$

where V is the velocity (ft/s) and ρ is the registered well log density RHOB (g/cm3) and the rest are constants.

Fig. 5b shows mudstone velocity-density cross-plots for wells in which such data and pressure measurements were available. Although there is scatter as a result of lithological variations and log quality, most

of the data fall within the boundaries defined by Bowers (2001) and Gardner (1974). These data give no clear indication of any unloading mechanism.

There are anomalous low-density/high velocity results that do plot outside of the Bowers-Gardner zone, all of which are found in mudstones close to or within the salt. These low values were interpreted as potentially attributable to the presence of salt, which is associated with low density readings within the clastic sediment (e.g. Lopez et al. (2004) and Zong et al. (2015)).

4. Hydro-mechanical models

4.1. Modelling approach

The models described in the present paper were developed using the finite element geological modelling software ParaGeo (Crook et al., 2018; Obradors-Prats et al., 2016, 2017a, 2017b, 2019) which enable the prediction of basin structural development while capturing the evolutionary stress and strain tensors, pore pressure and temperature distributions during basin history.

ParaGeo builds coupled, Thermo-Hydro-Mechanical (THM) models, adopting a staggered scheme with the coupling between the solved fields being performed at every flow in which each step encompasses on the order of a few hundred mechanical steps. The governing equations for (a) the mechanical and fluid flow fields are the linear momentum balance for a saturated medium containing a single fluid phase, and (b) Darcy’s single phase flow equation (see Appendix). The thermal field is modelled via the advective diffusion equation which is not described here as we have not accounted for any temperature dependent processes.

Our models simulate the deposition of clastic sediments on top of an initial salt volume. Each time a layer is deposited, a new mesh is generated to represent the sedimented material, deploying an adaptive remeshing algorithm. The gravity loading is gradually applied over the sedimentation stage to the new layer. During the evolution of salt and sediment deformation, a pinch out algorithm is used to eliminate and merge very thin elements, avoiding numerical instabilities.

The sediments are modelled using the critical state poro-elasto-plastic Soft Rock 4 model (SR4, e.g. Obradors-Prats et al., 2019) which can capture plastic strain hardening (compaction with strength increase) and plastic strain softening (dilation with strength decrease) depending on the stress path yielding location relative to the yield surface. Salt is modelled using the stress-dependent Herschel and Bulkley (1926) viscoplastic model. The equations for the constitutive models are provided in the Appendix.

In forward geomechanical models, salt flows as a result of differential topographic loading from the sediments deposited on top of the salt, with the predicted structures being difficult to constrain. In order to facilitate the prediction of a present-day structure consistent with its true geometry, a geomechanical restoration on the interpreted seismic section is performed in ParaGeo in order to obtain the shape of the depositional profiles required in the forward simulation to define the thickness variation of the sedimented layers (for further explanation see appendix section 8.4).

4.2. Model definition

4.2.1. 2D forward models

The initial geometry for the 2D plain strain model consists of an initial salt volume that is 15 km wide and 6 km high. A roller boundary condition is applied to the base and sides of the model so that perpendicular displacement to the boundaries is constrained whereas displacement tangential to the boundaries is allowed (Fig. 6). During the simulation 17 mudstone layers and 2 layers of isolated sand channels are sedimented which encompass Pliocene and Pleistocene ages (see appendix Table A 3). The depositional profiles for the sedimented layers

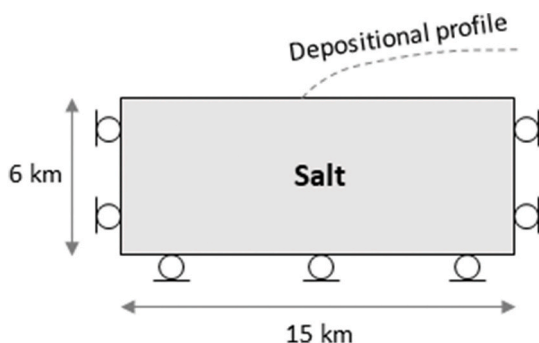


Fig. 6. Schematic of the initial model and boundary conditions.

were derived from a geomechanical restoration performed in ParaGeo (Figure A1) as described in the appendix section 8.4. Every time a new layer is deposited, the thickness at each horizontal coordinate given by the depositional profiles is added to the current top surface elevation (the depositional thickness at each location of the model is independent to the compaction of the previous layers).

The sediments' geomechanical properties were defined to be representative of each lithology and are summarised in Table A 1 within the Appendix. The material properties for the salt (Table A 2) were iteratively calibrated until the predicted present-day geometry was consistent with field observations.

The porosity-permeability relationships are defined using the Kozeny-Carmen model. A typical curve for sand is defined according to data from Hantschel and Kauerauf (2009). The curve for the mudstone layers was calibrated so that the pressure in the modelled sands matches the lowest pressure gradient from the multi-well data for B25 at the selected well location (Fig. 7, Figs. 8 and 9) because 1) those are the only data points that follow a water gradient and 2) most of the wells considered are consistent with such pressure regime. Water density was set as 1070 kg/m³ so that the hydrostatic gradient is consistent with the gradient estimated from pressure data. A water level boundary condition with a height relative to the seafloor surface is defined to provide the seafloor pore pressure prescribed value at each horizontal (X) coordinate of the model.

In addition to the base case model, four additional cases are simulated, considering heterogeneous permeability in Pleistocene03 and Pleistocene05 layers, which bound the isolated sand channels. In those

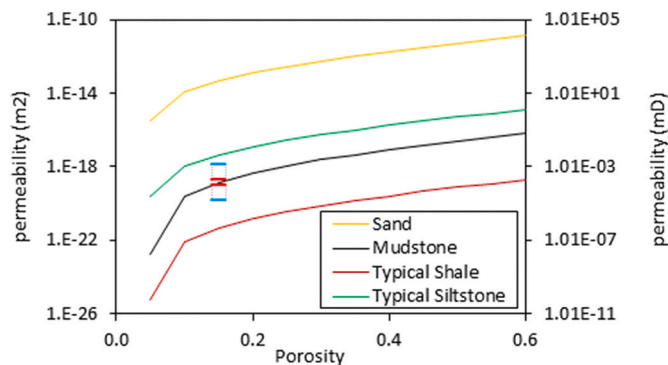


Fig. 7. Kozeny-Carmen porosity-permeability curves for sand and mudstone lithologies. Sand curve is defined using typical parameters from (Hantschel and Kauerauf, 2009). Mudstone curve is calibrated to fit pressure data at well location. Permeability anisotropy is considered with a horizontal to vertical permeability ratio of 5.0 for the sand and 1.5 for the mudstone. Typical curves for shale and siltstone according to (Hantschel and Kauerauf, 2009) are plotted for reference. The box plotted around the mudstone curve at porosities between 0.1 and 0.2 indicate the maximum (blue) and minimum (red) range of permeability contrast simulated for the cases run to explore the effect of heterogeneous permeability.

cases, for coordinates $X < 5900$ m (the left-most part of the layers), permeability is defined as being higher than that of the base case, whereas the permeability for coordinates such that $5900 \text{ m} < X < 11,000$ m (central part of the layers) is lower than in the base case. The permeability at the right-most part of the layers ($X > 11,000$ m) is the same as in the base case. The four cases considered permeability ratios between the high and low permeability regions of 2, 5, 10 and 100, respectively.

4.2.2. Column model

The 2D evolutionary model defined to reproduce the present-day field geometry incorporates the effect of disequilibrium compaction and salt-related tectonic deformation in generating overpressure. Furthermore, it incorporates the effects of the structural geometry in fluid-flow. To assess the relative contribution of disequilibrium compaction and tectonic deformation in both the present-day overpressure and porosities we developed a column model representative of the sedimentation at the well location in the 2D model. Such model does not include tectonic deformation and therefore will provide an approximation of the disequilibrium compaction component in the predicted pore pressure by the 2D model. In order to ensure that the same amount of sediments are deposited in both the 2D and the column models (ensure consistent amount of solids) the porosities predicted by the 2D model at the well location were decompacted to calculate the depositional thicknesses for each formation in the column model. All the remaining parameters and material properties are kept identical to the 2D model hence enabling comparisons.

5. Results

5.1. Results in base case model

5.1.1. Structural evolution

The predicted structural evolution by the 2D model is shown in Fig. 9 which is a result of the evolutionary salt deformational response to the weight of the sediments. The black arrows indicate the displacement directions within the salt body. At the start of simulation, the sediments do not cover the entire length of the salt top horizon so that as new layers are being deposited, the sediments sink downwards and salt evacuates from locations below the sediments, flowing towards the southern part of the model and then upwards following a pseudo semi-circular pathway. This leads to the formation of a salt wall/diapir adjacent to the mini-basin flank, with flow mainly in the upward direction until the last three deposition events during which sediments cover the whole of the model length.

The eight isolated sand channels, deposited in two sets of four channels with a mudstone layer in between (Table 2), span approximately half of the model length (the region included in the seismic section) as defined by the sedimentation thickness profiles in Figure A 2 c.

Our model has captured the observed diapir/salt wall covered by young sediments next to the mini-basin flank, a salt bulge at the base of the diapir wall and a synclinal shape of the sediments with onlap on the salt wall. The model overpredicted sediment sinking, resulting in a larger amount of salt flowing towards the diapir/salt wall top and generating additional horizontal push from the salt towards the north. Also, the thickness of the sediments covering the top of the diapir/salt wall plateau is overpredicted. Nonetheless such degree of mismatch is expected when considering the degrees of freedom in a predictive evolutionary geomechanical modelling approach involving salt reologies.

5.1.2. Stress and overpressure distributions

The predicted overpressure distribution in mini-basin sediments is shown in Fig. 11 (c) and (e). The maximum overpressure developed in the deepest sections of the mini-basin depocenter at the northern model

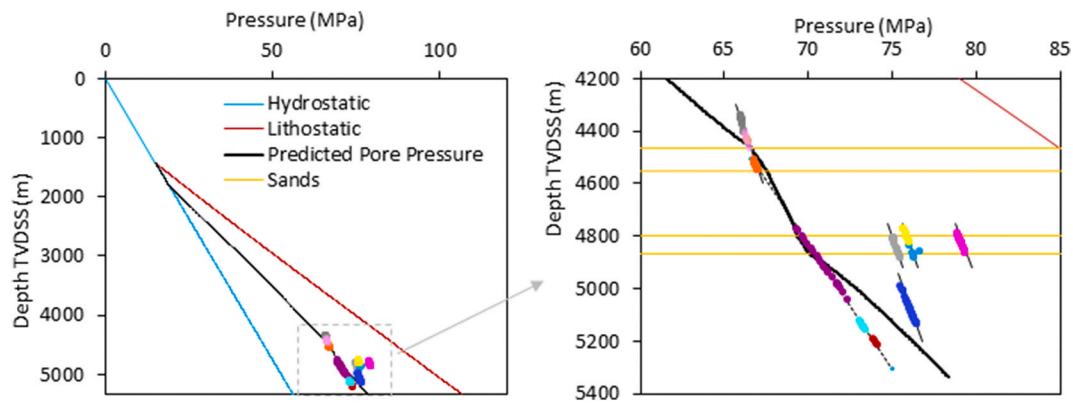


Fig. 8. Comparison of predicted pore pressure after calibration with pressure data in sands. The colours in the pressure data correspond to different wells as indicated in Fig. 4. The yellow horizontal lines show the top and bottom depths of the two sand channels intersected by the well in our model. The well location in our model is shown in the present-day geometry of Fig. 9.

boundary is 40.8 MPa. In this location, the sedimentation rate is faster relative to other model locations, leading to larger overpressure due to disequilibrium compaction. This is reflected in the convex-up shape of the overpressure contours, so that if overpressure is measured across a layer following a direction parallel to the bedding, overpressure decreases from North to South.

The vertical and horizontal effective stress distributions in the sediments are shown in Fig. 11 (a) and (b) respectively. Both plots show a general trend of effective stress increase with depth, with a lower stress gradient towards the North (e.g., the 30 MPa value is reached at ca. 4600 m depth at a location close to the middle of the model length, whereas at the model's northern boundary, it is not reached until 5400 m depth, consistent with the relatively larger overpressure gradient towards the North (overpressure decreases the effective stresses).

The red boxes in those figures show locations where there are local reductions in effective stress. The horizontal effective stress contours show a local reduction of 3 MPa above the salt bulge. This is due to the stress arching effect that the bulge induces on sediments. On the other hand, the vertical effective stress contours show a reduction in the sediments adjacent (<700 m distance) to the salt diapir wall. For example, the white point within the red box in Fig. 11 (a) is at 2.2 km depth below mudline, has a vertical effective stress of 15.0 MPa and an overpressure of 12.9 MPa whereas the pink point which is at the same depth, located adjacent to the salt wall at a distance of 673 m, has a vertical effective stress of 10.3 MPa with an overpressure of 11.6 MPa (lower overpressure and lower effective stress than the white point). Such reduction in vertical effective stress is attributed to the drag that the salt exerts on adjacent sediments as the salt diapir raises upwards.

The horizontal to vertical effective stress ratio contours reveal that most of the basin sediments are in horizontal compression, showing values larger than the value for uniaxial burial conditions (k_0 value of 0.81 in Fig. 11 (d)). In addition, sediments next to the salt diapir wall show values larger than 1.0 (hot colours in Fig. 11 (d)), meaning that horizontal effective stress exceed the vertical effective stress in those locations. This is supported by the maximum principal stress directions which display a sub-horizontal direction in locations with warm colours and a sub-vertical direction otherwise. It can be observed that the sediments above the diapir top (southern part of the model) are in horizontal extension, which is attributed to the horizontal stretch generated by both (a) the diapir top expanding horizontally in the most recent period in the basin history and (b) the arching-related stretch resulting from the opposite kinematic directions of the sediments sinking in the mini-basin flank and sediments being held by the rising diapir top.

5.1.3. Overpressure, porosity and stresses in sand channels

In this section the discussion will focus on the pore pressures in the isolated sand channels. To that end the results at each mesh element

within sand channels have been extracted for processing.

In Fig. 12 (a) and (b) porosity and overpressure in the sand channels are plotted with depth. The overpressure is the same for all elements in each individual sand channel because the high permeability and the relative short distance facilitate a rapid distribution of overpressure within each sand body. The overpressure in different sands ranges from 16.5 MPa in sand08 to 27.9 MPa in sand01. Larger overpressure is observed for older and deeper sands (e.g., sands 01 to 03 in cold colours) compared to younger, shallower sands (e.g., sands 06 to 08 in warm colours). In addition, overpressure increases for sands located towards the North, consistent with the overpressure contours shown in Fig. 11. The plot shows that the model has captured overpressure compartmentalisation in that different sand channels have different overpressure magnitudes at the same depth. The maximum difference in pressure for a given depth is 5.6 MPa between sands 04 and 05 which are located at 2.55 km from each other. The porosity plot shows that porosities in all sand channels are larger than the NCT. The high overpressure generated by disequilibrium compaction facilitated porosity preservation with a maximum difference between the average porosity for a given sand channel to the NCT of 3 porosity units observed for sand01 (Sathar and Jones, 2016).

Fig. 12 (c), (d) and (e) shows cross plots of porosity, overpressure, and effective stress ratio values within the sand channels. Those provide information that helps to interpret the effect of tectonic deformation on porosity and overpressure generation, and the relative contribution of tectonic deformation and disequilibrium compaction in generating the observed overpressure magnitudes. In Fig. 12 (c), it is clear that porosity decreases as effective stress ratio increases for each set of sand channels of the same age (cold colours for the oldest set of sand channels and warm colours for the youngest one). This indicates that the compressional tectonic deformation due to salt halokinesis (which increases horizontal effective stress and hence increases the effective stress ratio) has a role in decreasing porosity in the sand channels.

From the overpressure and effective stress ratio cross plot (Fig. 12 (d)) no clear correlation can be established, indicating that tectonic deformation may be of second order importance as an overpressure generation mechanism in the present scenario. In Fig. 12 (e), the average values show a correlation of porosity preservation with high overpressure for each set of sand channels of same age, which is indicative of disequilibrium compaction. Nonetheless it is noted that sands 04 and 08 do not follow the same trend. Sands 04 and 08 are the channels most proximal to the flank for each respective sand channel set and have relatively high reliefs. The flow pathways (Fig. 11 (e)) reveal that sand 04 receives flow from the younger sand 07 and at the same time sand 04 transfers some pressure to sand 08. This transfer of pressure has influenced the overpressure-porosity relationship for those sands so that they do not follow the simple disequilibrium compaction trend. The complex

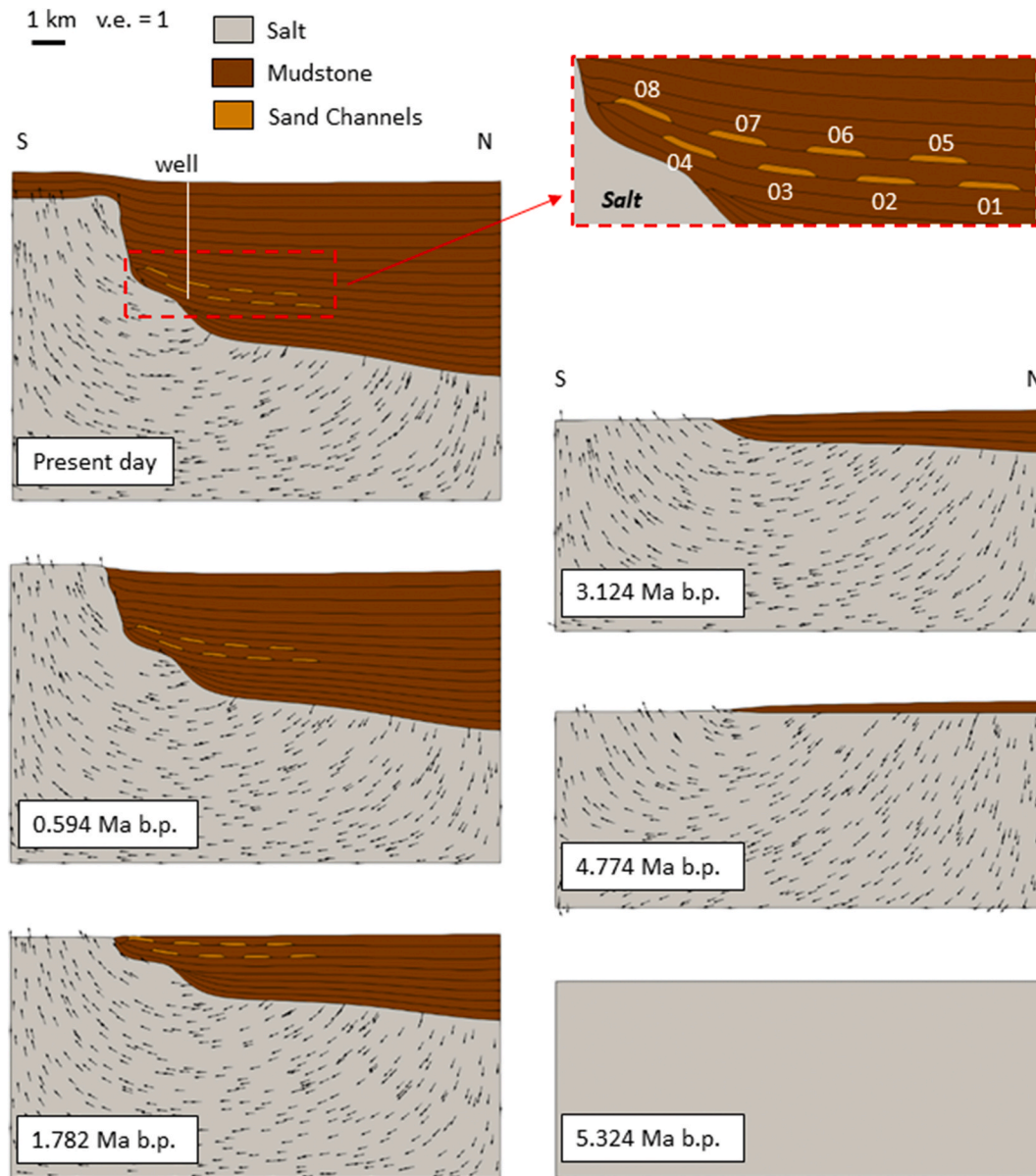


Fig. 9. Predicted geometries at selected times. The black arrows indicate the displacement directions within the salt. The isolated sand channels in the model are numbered here to facilitate reference in the text. The predicted present-day geometry is compared to the present-day geometry defined from the seismic interpretation in Fig. 10. The model has predicted a first order approximation of the observed salt-sediment interface and sediment features, although some differences are noticeable.

regime involving fluid flow between different sand channels is a result of the increasing overpressure towards the North and the increasing dip of the sand channels towards the salt wall. Hence fluid flows from sands with larger overpressure (e.g. Sand 07) to sands with lower overpressure (e.g. Sand 04) and the relatively large dip of the sands adjacent to the salt facilitates pressure transfer between different depths.

5.2. Comparison with 1D: Disequilibrium compaction vs. tectonic Deformation

To enable assessment of the relative contribution of disequilibrium compaction and tectonic deformation in overpressure generation and porosity preservation, a uniaxial compaction column model for the well shown in Fig. 9 is simulated. This model accounts solely for disequilibrium compaction generated overpressure.

The results for this model, in terms of overpressure and porosities, are compared to the 2D model results in Fig. 13. It is observed that the

2D model predicts 1.4 MPa more overpressure than the uniaxial compaction column model at the top of the younger sand (~4400 m depth), which is seven percent of the total overpressure in the 2D model. This indicates the relatively low contribution of tectonic deformation compared to disequilibrium compaction as an overpressure generation mechanism at the well location.

The porosities predicted by the uniaxial compaction column model are larger than the porosities in the 2D model. For example, at 3.3 km depth the porosity for the column model is 0.186 compared to 0.143 for the 2D model. This is because of the additional tectonic compaction that is uniquely captured in the 2D model and contributes to porosity reduction. Because the same mass of solids are deposited in the two models (required to enable quantification of the contribution by disequilibrium compaction and tectonic-induced overpressure generation), the lack of tectonic compaction resulted in a slightly thicker, less compacted mudstone overburden above the youngest sand channel in the column model (and hence a slight increase in the sand channel depth

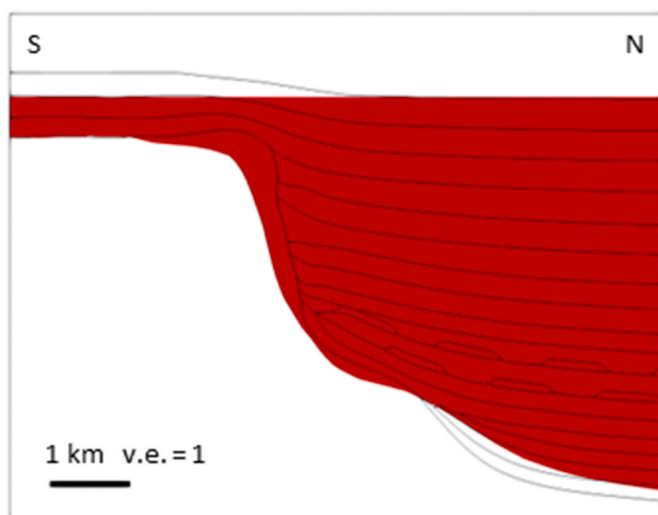


Fig. 10. Comparison of predicted geometry (black lines) with the present-day geometry defined according to a seismic interpretation on the N–S line shown in Fig. 1 (red solid surface).

Table 2

Summary of results for the simulated cases considering heterogeneous permeability in Pleistocene03 and Pleistocene05 mudstone layers with different maximum to minimum permeability ratios. For reference, the permeability for the cases with the maximum and minimum permeability ratio values are plotted in Fig. 7 with blue and red lines, respectively.

Minimum Permeability (m ²)	Maximum Permeability (m ²)	Permeability Ratio	Maximum Overpressure Difference (MPa)
1.40E-19	1.40E-19	1	5.61
1.40E-20	1.40E-18	100	18.14
4.20E-20	4.20E-19	10	12.25
5.60E-20	2.80E-19	5	10.03
9.32E-20	1.86E-19	2	7.66

relative to the 2D model).

5.3. Effects of heterogeneous permeability

Four cases considering heterogeneous permeability in the Pleistocene03 and Pleistocene05 mudstone layers are simulated to investigate the potential effect of permeability distribution in overpressure compartmentalisation between the sand bodies. In these cases, the permeability at locations close to the salt wall is increased relative to the base case, whereas permeability at locations further from the salt wall is decreased relative to the base case (Fig. 14 (a)).

Fig. 14 (b) and (c) shows the porosity and overpressure results in the sand channels, for the case with the largest maximum to minimum permeability ratio. By comparing the results in Fig. 14 with the results for the base case shown in Fig. 12 (a) and (b), it is noted that the heterogeneous permeability has generally led to larger overpressures and larger porosities in sand channels located in the low permeability zone relative to the base case, whereas for sand channels located in the high permeability zone, overpressure and porosities are decreased relative to the base case.

The maximum overpressure difference at the same depth between two sand channels has also increased relative to the base case. In this case the heterogeneous permeability has enhanced overpressure compartmentalisation leading to a maximum overpressure difference of 18.14 MPa between sand 01 and sand 03.

Table 2 summarizes the results in terms of the maximum overpressure difference at a given depth between two sand channels for the

different cases with heterogeneous permeability considered. It is observed that as the maximum to minimum permeability ratio increases the maximum overpressure difference also increases. This indicates that permeability distribution is a key factor controlling overpressure compartmentalisation in isolated sand channels. The results show that a permeability ratio of 5 is required to obtain an overpressure difference of 10 MPa, equivalent to the maximum overpressure difference measured in the data.

6. Discussion

6.1. Overpressure generation mechanisms

The well data from Magnolia field suggest that there are different mechanisms that contributed to generate the observed overpressure. The well logs show trends that are consistent with disequilibrium compaction which is interpreted to be of first order of importance in the region. This is expected given the fast sedimentation rates and the mudstone-dominated sedimentary column. The presence of oil and gas pressure gradients in the considered B-25 sands indicate that there is a component of buoyant pressure due to the presence of hydrocarbons. Nonetheless, log-based interpretation could not give accurate quantification of the different overpressure generation mechanisms. Diagenesis and aquathermal expansion may be ruled out given the low maximum bottom hole temperature reached in the field (~70 °C) and the short time frame for the diagenetic reactions to develop. The data shows that some sand levels are hydraulically connected because the pressure measurements plot on a common hydrostatic-parallel or hydrocarbon gradient, so that pressure transfer (potentially both lateral and vertical) is present. Assessment of the quantitative contribution of the different processes in the observed overpressure is rather difficult via analytical or data-driven methods and hence we use our numerical models to provide additional insight.

Our 2D coupled models incorporate overpressure being generated by two main mechanisms: disequilibrium compaction and tectonic deformation. Pressure transfer is also allowed in the simulations but given that our models considered isolated sand channels bounded by low permeability mudstones, this mechanism is of secondary importance in the results as it mainly occurs within each sand channel. As disequilibrium compaction and halokinesis-related tectonic deformation are coeval during the history of the basin, we built a column model simulating the sediment deposition at the well location (without tectonic deformation) to enable assessment of the relative contribution of disequilibrium compaction and tectonic-induced overpressure in the predicted overpressure by the 2D model. The difference between the results from the 2D mini-basin model and the column model suggests that tectonic deformation has a secondary role in generating overpressure and that disequilibrium compaction is the dominant overpressure generating mechanism. This is reinforced by the shape of the predicted overpressure contours, which show a trend of increasing overpressure towards the depocenter (where there is more disequilibrium compaction) and did not show any local overpressure increase near the salt wall. Furthermore, it should be noted that the interpreted salt geometry from seismic data suggests a rather moderate salt-related tectonic compression to the adjacent sediments. Such low-degree of tectonic strain combined with the synchronous fast deposition of mud-dominated lithologies facilitated any potential effects of the salt-related tectonic deformation on overpressure to be overridden/masked by disequilibrium compaction. It would be expected that a salt diapir with more growth and more diapir head expansion in the horizontal direction than the case considered here would lead to a larger amount of tectonic strain in the adjacent sediments and hence more overpressure generation. There are other examples in the literature that used numerical modelling to demonstrate the importance of salt-induced tectonic deformation as an overpressure generation mechanism in passive basins where the diapirs have experienced more growth than in the

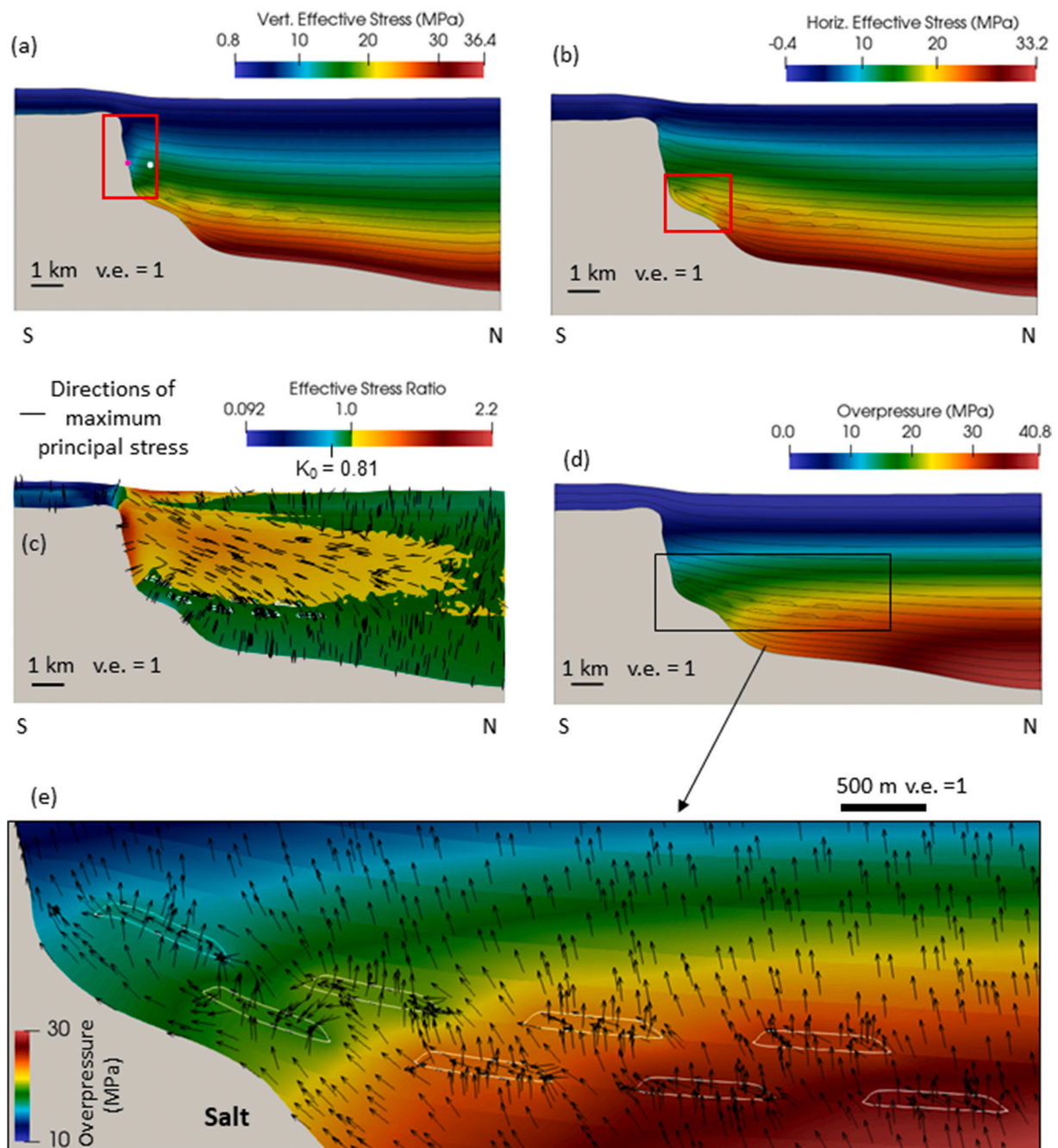


Fig. 11. Vertical effective stress (a), horizontal effective stress (b), effective stress ratio contours (c) and overpressure (d and e) in the mini-basin sediments. Pink and white points in figure (a) are displayed to facilitate discussion in the text. Lines in figure (c) indicate direction of the maximum principal stress. Arrows in figure (e) indicate flow direction vectors.

scenario considered in the present paper (e.g. Luo et al., 2017; Nikolinakou et al., 2018). In those examples there is a greater impact of salt tectonics on adjacent sediments and hence the role of salt-related tectonic deformation as an overpressure generation mechanism becomes more important.

Comparison of the results from the 2D model and the column model has also shown that salt-induced tectonic deformation leads to porosity decrease, driven by the increased horizontal effective stress. This has implications for pore pressure prediction in salt-tectonics scenarios using porosity-based methods (e.g., the Equivalent Depth Method) because tectonic compaction has contributed to decrease porosity beyond that predicted by purely vertical effective stress; this results in a porosity-depth trend that is closer to the normal compaction trend,

leading to a lower predicted pore pressure by those methods (Obradors-Prats et al., 2016, 2017a; Luo et al., 2017).

6.2. Pressure compartmentalisation

Pressure data for Magnolia field wells shows that there is pressure compartmentalisation between some sand intervals (i.e., different pressure magnitude in relatively proximal sands measured at the same depth) as well as hydraulic connectivity between some sands at different depths (the pressure data points follow the same pressure gradient). Both scenarios have been observed between sand layers from different formations (Sathar and Jones, 2016) as well as between different sand layers in the same formation, as discussed in the present paper for B-25.

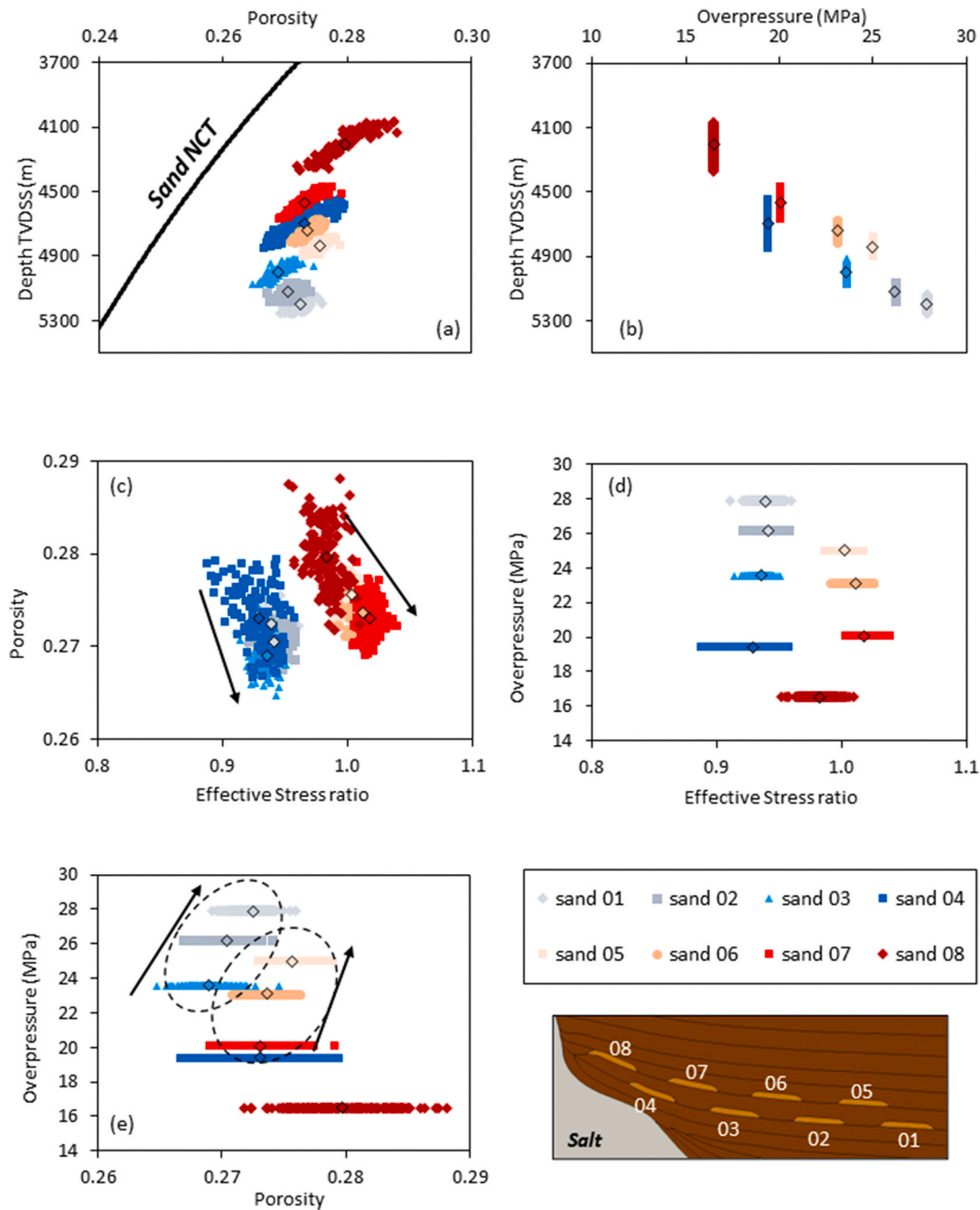


Fig. 12. Results obtained at each sand channel finite element. Cold colours are assigned for the oldest set of sand channels whereas warm colours show the results for the youngest set of sand channels. Empty diamonds show the average value in each sand channel. Porosity (a) and overpressure (b) as a function of depth in each sand channel. Porosity as a function of effective stress ratio (c), overpressure as a function effective stress ratio (d) and overpressure as a function of porosity (e). The arrows in figures (c) and (e) indicate the trends discussed in the text. The two ellipsoids in (e) indicate the sands considered to determine trends (these exclude sand 04 and sand 08 which are located at the mini-basin flank as shown in Fig. 9).

The reservoirs of the Magnolia Field consist in deepwater submarine sand channels deposited on a mudstone dominated environment (Kane et al., 2012).

The configuration of deepwater channel systems can in principle allow both connectivity and compartmentalisation in all directions. This is the case with the reservoirs in the Magnolia Field where the measured pore pressures indicate both scenarios. To better establish the connectivity between these channels, higher resolution seismic data are required.

We have simulated the deposition of isolated sand channels bounded by mudstones to allow modelling of pressure compartmentalisation and investigate the required permeability contrasts in bounding mudstones

to explain the observed pressure differences in the sands. Our base-case model has captured overpressure compartmentalisation with a maximum difference of 5.6 MPa in overpressure between sand channels at the same depth with overpressure increasing towards the North (towards the depocenter). The pressure differences are attributed to the faster sedimentation rates and increasing overburden thickness towards the North. In our model the overburden thickness measured from the top of the youngest sands at the centre of each sand channel is 3370 m for sand 5, 3273 m for sand 6, 3095 m for sand 7 and 2728 m for sand 8. Given that the overburden above the youngest sand channels is deposited over a period of 1.98 Ma, this leads to sedimentation rates varying from 1700 m/Ma in sand 5 to 1377 m/Ma in sand 8, thus generating

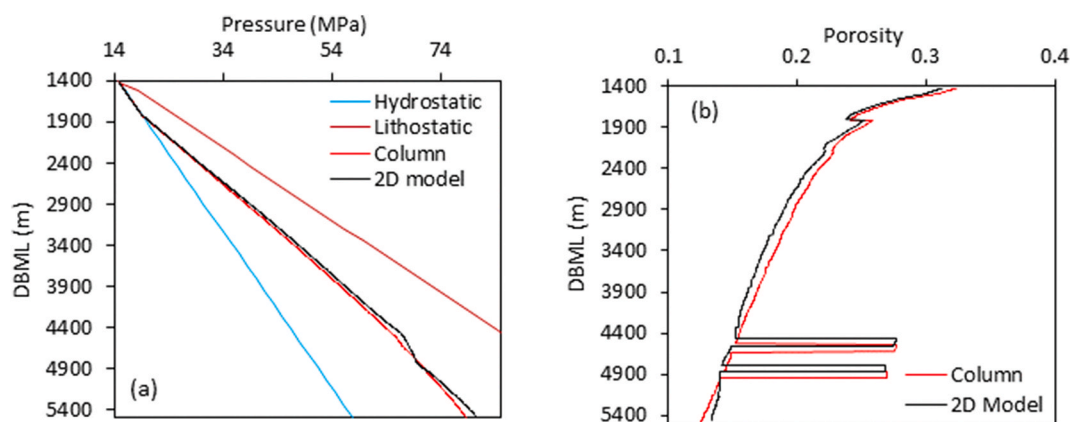


Fig. 13. Comparison of pore pressure and porosity predictions for the 2D model at the well location shown in Fig. 9 and the corresponding uniaxial compaction column model.

more overpressure due to disequilibrium compaction for sand channels closer to the depocenter. The sand channels are bounded by mudstones which have low permeability leading to a poor hydraulic connectivity between isolated sand channels. This, in addition to the relatively short timescale (less than 2 Ma), drives significant pore pressure differences between reservoirs located at relatively short distance.

The pressure data for B-25 formation in the Magnolia Field show a difference of 10 MPa in different wells at the same depth. Our calibrated model has shown a pressure difference of 5.6 MPa assuming a homogeneous porosity-permeability relationship for mudstone formations in all the domain. We have undertaken four extra simulation cases which considered heterogeneous permeability across the two formations that bound the sand channels. The modelling shows that, given the fast sedimentation rates, relatively small permeability contrasts lead to an increased difference in the overpressure between different sand channels (see the variations in permeability considered indicated by the blue and red lines in Fig. 7). In our study a permeability ratio of 5 is sufficient to produce the observed pressure difference of 10 MPa between different sand channels. Heterogeneity of permeability can result from variations in mudstone clay fraction, changes in mineralogy, changes in fabric, etc. It should be noted that the cases analysed are rather conservative as heterogeneity in permeability is considered only in two formations (Pleistocene03 and Pleistocene05).

The simulation of isolated sand channels in our models has enabled the analysis of trends among various parameters such as depth, overpressure, porosity and effective stress ratio from sands located at different structural locations in the mini basin. The results have confirmed significant role of fast sedimentation rates in generating overpressure by disequilibrium compaction and highlighted the impact of tectonic deformation and horizontal effective stress in decreasing porosity. It should be noted however that these trends are to some extent influenced by the complex fluid flow patterns between the different sand channels at different structural locations within the mini-basin, with varying overburden thicknesses and dips. This is reflected by the variability in the values obtained for each sand channel.

6.3. Additional considerations on the modelling results

Pressure data shows a buoyant component in pore pressure due to the presence of hydrocarbons (both oil and gas). However, the models presented in this work do not account for overpressure as a result of hydrocarbon generation and migration. This is because the simulations were conducted at a time when petroleum system modelling and multiphase flow functionalities were not available in ParaGeo. In addition, we lack data to constrain the location and timing of hydrocarbon generation as well as the migration pathways. However, it is unlikely that hydrocarbon generation and migration, in our case, make

significant contributions to overpressure beyond buoyancy. This is because local hydrocarbon generation is unlikely near the reservoir units, given the reservoir temperature of 70 °C.

Our 2D models have successfully captured pressure compartmentalisation in isolated sand channels and improved our understanding of the potential factors influencing pressure compartmentalisation in the Magnolia field. However, the data reveals a more complex scenario where certain sand intervals are compartmentalised whereas others are hydraulically connected. This complexity falls outside the scope of this work and has not been accounted for in our model. To capture this complexity a 3D geometry with sand connections at different depths would be necessary. It should be noted however that this level of complexity cannot be observed through seismic data and is rather difficult to anticipate. Therefore, models that incorporate such scenarios may be useful for proof of concept but are unlikely to be available for predictive purposes.

The analysis of the pressure data for reservoir B-25 shows that wells closer to a salt wall have a larger reservoir overpressure. This indicates that salt exerts a first order control on overpressure. However, our model has not captured a notable tectonically-induced overpressure increase near the salt wall despite predicting an evolutionary geometry that overestimates the horizontal push from the salt to the adjacent sediments at present day (as illustrated in Fig. 10). Consequently, the model likely overestimates the impact of tectonic strain. This suggests that salt may have a local impact on overpressure beyond the tectonic strain induced by salt, potentially through a mechanism that is not accounted for in our models. One possible explanation could be the presence of sub-seismic thin salt beds in the overburden, which may have formed due to salt precipitation in small fractures, leading to a decrease in permeability. This could result in a greater degree of disequilibrium compaction and an enhanced pressure compartmentalisation. However, to support the plausibility of this hypothesis, additional data is required.

7. Conclusions

We have investigated overpressure development and overpressure compartmentalisation in the Magnolia Field, Gulf of Mexico using a multidisciplinary approach including petrophysical analysis, reservoir characterisation, seismic interpretation and coupled, forward geomechanical modelling. We conclude that.

- 1) Log-based interpretation suggests that overpressure in the Magnolia Field was generated mainly by disequilibrium compaction. This is consistent with the fast deposition of low permeability, mud-rich sedimentary sequences. However, comparison of 2D model results with a 1D column model show that seven percent of the total overpressure is due to salt tectonics in such scenario with moderate non-

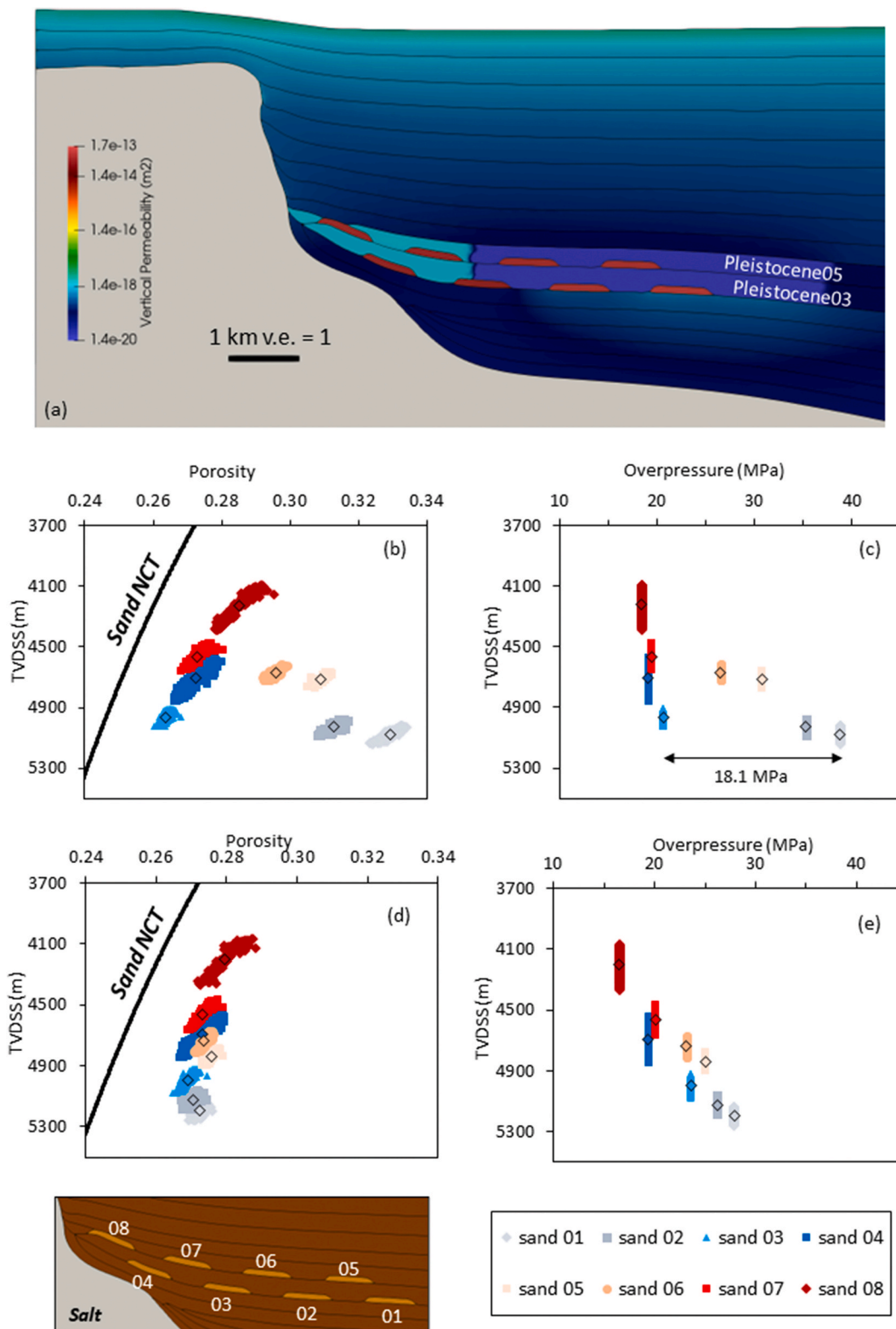


Fig. 14. (a) Vertical permeability distribution for the case considering heterogeneous permeability in Pleistocene03 and Pleistocene05 layers with a maximum to minimum permeability ratio of 100 in such layers. Note that in such layers the permeability is not a function of porosity. Porosity (b) and overpressure (c) results in each sand channel for the case with heterogeneous permeability in Pleistocene03 and Pleistocene05 mudstone layers with a maximum permeability to minimum permeability ratio of 100 (case with the largest permeability contrast considered in this study). Porosity (d) and overpressure (e) from base case previously shown in Fig. 12 are included to facilitate comparisons.

vertical salt push to adjacent sediments. Tectonic compression also reduces porosity close to the salt dome.

- 2) Hydraulic connectivity between sands in channel reservoir packages is complex and variable, both laterally and vertically. Vertical compartmentalisation is related to the presence and extent of inter-reservoir mudstone packages, while horizontal compartmentalisation is due to lithological heterogeneity plus variations in small-scale sedimentary structures related to the sedimentary environment and salt tectonics. Such sedimentological heterogeneities are important in terms of fluid flow and overpressure development but are inherently unpredictable.
- 3) Pore pressure differences of up to 10 MPa are measured in different wells at the same depth within the same reservoir (B-25). 2D hydro-mechanical models show that pressure compartmentalisation relates to local differences in sedimentation rates and the low permeability of the bounding mudstones that isolate individual channel sands. Slight changes in permeability heterogeneity can lead to increased pressure compartmentalisation, implying that local variations in sediment grain size or fabric may have a first order control in overpressure compartmentalisation in rapidly deposited, geologically young sediments.

Appendix

Governing Equations

For the mechanical field we solve the linear momentum balance equation for a saturated porous medium containing a single fluid phase which is written as [Lewis and Schrefler \(1998\)](#).

$$\mathbf{L}^T(\boldsymbol{\sigma}' - \alpha(\varphi)\mathbf{m}p_f) + \rho_b\mathbf{g} = 0 \tag{A1}$$

Where \mathbf{L} is the standard continuum mechanics differential operator, $\boldsymbol{\sigma}'$ is the effective stress tensor defined as:

$$\boldsymbol{\sigma}' = \{ \sigma'_x \quad \sigma'_y \quad \sigma'_z \quad \tau_{xy} \quad \tau_{yz} \quad \tau_{zx} \}^T \tag{A2}$$

σ'_x, σ'_y and σ'_z are the normal stresses orthogonal to planes x, y and z respectively, τ_{yz}, τ_{zx} and τ_{xy} are the tangential stresses acting in planes x, y and z respectively, $\alpha(\varphi)$ is the Biot coefficient as a function of porosity which in the present paper is assumed $\alpha(\varphi) = 1$, p_f is the fluid pressure and \mathbf{m} is the hydrostatic unit tensor which is defined as:

$$\mathbf{m} = [1 \quad 1 \quad 1 \quad 0 \quad 0 \quad 0]^T \tag{A3}$$

ρ_b is the saturated bulk mass density defined as:

$$\rho_b = (1 - \varphi)\rho_s + \varphi\rho_f \tag{A4}$$

ρ_s and ρ_f are the solid grain and fluid densities respectively, φ is the porosity and \mathbf{g} is the gravitational vector.

The effective stress is defined as:

$$\boldsymbol{\sigma}' = \boldsymbol{\sigma} - \alpha(\varphi)\mathbf{m}p_f \tag{A5}$$

Where $\boldsymbol{\sigma}$ is the total stress tensor.

We model fluid transport over geological time scales by means of Darcy's flow equation which is defined in [Lewis and Schrefler \(1998\)](#) as:

$$\text{div} \left(\frac{\mathbf{k}(\varphi)}{\mu_f} (\nabla p_f - \rho_f \mathbf{g}) \right) = \left(\frac{\varphi}{K_f} + \frac{(\alpha(\varphi) - \varphi)}{K_s} \right) \frac{\partial p_f}{\partial t} + \frac{\alpha(\varphi)}{1 - \varphi} \frac{\partial \varphi}{\partial t} \tag{A6}$$

where K_s and K_f are the solid grain and fluid stiffness respectively, μ_f is the fluid viscosity, $\mathbf{k}(\varphi)$ is the permeability tensor which is a function of porosity. Note that the last term represents fluid flow due to compaction (porosity change) and provides the coupling between fluid flow and mechanical fields.

8.2 Stress invariants definition

The effective mean stress (p') and deviatoric stress (q) may be defined as a function of principal effective stresses (σ'_1, σ'_2 and σ'_3) as:

Declaration of competing interest

The authors declare that they have no known competing financial interests or personal relationships that could have appeared to influence the work reported in this paper.

Data availability

The authors do not have permission to share data.

Acknowledgements

These investigations were conducted as part of the GeoPOP4 industry supported research consortium funded by BP and Petrobras. Durham and Newcastle Universities thank these companies for funding this research. The authors want to thank the two anonymous reviewers for their constructive comments which helped to improve the present paper. Data used in this project were provided by ConocoPhillips.

$$p' = \frac{1}{3}(\sigma'_1 + \sigma'_2 + \sigma'_3) \tag{A7}$$

and

$$q = \sqrt{\frac{(\sigma'_1 - \sigma'_2)^2 + (\sigma'_1 - \sigma'_3)^2 + (\sigma'_2 - \sigma'_3)^2}{2}} \tag{A8}$$

here we adopt positive sign for compressional stresses and negative sign for tensional stresses.

Constitutive models

Mudstone and sand channels

The mudstone and sand channel behaviour is modelled via the SR4 model (e.g., Obradors-Prats et al., 2019), a non-associative Cam Clay type model based on critical state principles. Such poro-elasto-plastic model is capable to simulate strain hardening (increase in strength due to compaction), strain softening (sediment strength decrease with dilation) and continuous shear with constant volume and stresses at critical state (Wood, 1990).

The strength of the material is represented by the yield surface which is defined in the p' - q plane as:

$$f(p', \varepsilon_v^p) = g(\theta, p')q + (p' - p_t)\tan \beta \left[\frac{(p' - p_c)}{(p_t - p_c)} \right]^{\frac{1}{n}} \text{ for } p' \leq p_{peak} \tag{A9}$$

and

$$f(p', \varepsilon_v^p) = [g(\theta, p')]^2 q^2 - M^2 p_{peak}^2 \left[1 - \frac{(p_{peak} - p')^2}{(p_{peak} - p_c)^2} \right] \text{ for } p' > p_{peak} \tag{A10}$$

where p_t in the tensile intercept of the yield surface with the hydrostatic axis, p_c is the pre-consolidation pressure or compressive intercept of the yield surface with the hydrostatic axis, p_{peak} is the effective mean stress corresponding to the peak q value of the yield surface, M is the slope of the line that intersects the origin and the yield surface at peak q value, β and n are material constants defining the shape of the yield surface on the p' - q plane, θ is Lode's angle and $g(\theta, p')$ is a function that controls the shape of the yield surface in the deviatoric plane defined as:

$$g(\theta, p) = \left[\frac{1}{1 - \beta^\pi (p')} \left(1 + \beta^\pi (p') \frac{r^3}{q^3} \right) \right]^{\alpha^\pi} \tag{A11}$$

with

$$\beta^\pi(p') = \beta_0^\pi \exp\left(\beta_1^\pi p' \frac{p_{c0}}{p_c} \right) \tag{A12}$$

Where α^π , β_0^π and β_1^π are material constants defining the shape of the yield surface in the deviatoric plane and p_{c0} is the initial pre-consolidation pressure and

$$r^3 = \frac{9}{2} \mathbf{s} : \mathbf{s} : \mathbf{s} = \frac{27}{2} J_3' \tag{A13}$$

where \mathbf{s} is the deviatoric stress tensor.

The non-associative flow potential surface is defined with a function similar to the yield surface with different material constants and no deviatoric plane correction term as:

$$\psi(p', \varepsilon_v^p) = q + (p' - p_t)\tan \varphi \left[\frac{(p' - p_c)}{(p_t - p_c)} \right]^{\frac{1}{m}} \text{ for } p' \leq p_{\psi peak} \tag{A14}$$

and

$$\psi(p', \varepsilon_v^p) = q^2 - M_{\psi}^2 p_{\psi peak}^2 \left[1 - \frac{(p_{\psi peak} - p')^2}{(p_{\psi peak} - p_c)^2} \right] \text{ for } p' > p_{\psi peak} \tag{A15}$$

where φ and m are material constants defining the shape of the flow potential surface and M_{ψ} is the slope of the line that crosses the origin and the flow potential surface at q peak value and $p_{\psi peak}$ is the effective mean stress value for the flow potential surface at q peak value. Note that if $n = m$ then $p_{peak} = p_{\psi peak}$ and therefore the critical state is located at the peak q value of the yield surface.

When stress paths intersect the yield surface plastic strains will develop leading to hardening or softening depending whether the yielding location is on the compaction side or shear side of the yield surface, respectively. The evolution of the yield surface during hardening and softening is controlled

by the hardening law defined as:

$$p_c = p_{c0} \exp \left[- \frac{v \varepsilon_v^p}{(\lambda - \kappa)} \right] \tag{A16}$$

and

$$p_t = p_{t0} \exp \left[- \frac{v (\varepsilon_v^p)_{\max}}{(\lambda - \kappa)} \right] \tag{A17}$$

where v is the specific volume, p_{t0} is the initial tensile intercept, λ and κ are the slope of the normal compression line and the slope of the unloading-reloading line in the $v - \ln p'$ plane, and ε_v^p is the volumetric plastic strain and $(\varepsilon_v^p)_{\max}$ is the maximum dilatational volumetric plastic strain.

Stress paths moving inside the yield surface are governed by elasticity with the bulk modulus being defined by the poroelastic law:

$$K = K_{dep} + (1 - A_{un}) \frac{p_c}{\kappa} + A_{un} \frac{p'}{(1 - \varphi)\kappa} \tag{A18}$$

where K_{dep} is the bulk modulus at deposition and A_{un} is a poroelastic constant.

Salt

Salt is modelled using the stress-dependent Herschel-Bulkley viscoplastic model described by the following equation:

$$\dot{\varepsilon}_c = \left(\frac{q - q_y}{3K_{visc}} \right)^{\frac{1}{n_{visc}}} \quad \text{for } q > q_y \tag{A19}$$

where $\dot{\varepsilon}_c$ is the effective creep viscoplastic strain rate, q_y is the yield strength, K_{visc} and n_{visc} are material constants. In such model the more the deviatoric stress exceeds the yield strength, the faster the viscoplastic strain rate thus enhancing salt flow.

Table A 1

Geomechanical properties for mudstone and sand lithologies. Porosity-permeability curves are provided in a separate figure. Note that mudstone depositional porosity is defined with a low value in order to achieve a depositional bulk density larger than that of the salt and therefore promote sinking and avoid unrealistic positive relief in basin sediments at initial stages. Nonetheless the normal compaction trend (NCT) is calibrated so that it fits the compaction trend porosity data from (Ewy et al., 2020) at depths below 1000 m.

Property	Symbol	Units	Mudstone	Sand
Grain Stiffness	K_g	MPa	30,000	30,000
Grain Density	ρ_g	$\frac{Kg}{m^3}$	2700	2700
Depositional Porosity	φ_0	-	0.35	0.44
Poisson's ratio	ν	-	0.3	0.25
Depositional Bulk Modulus	K_{dep}	MPa	10	10
Unloading line slope	κ	-	0.01	0.01
Poroelastic constant	A_{un}	-	0	0
Normal compression line slope	λ	-	0.09	0.1
Depositional pre-consolidation pressure	p_{c0}	MPa	-0.5	-0.5
Tensile intercept	P_{t0}	MPa	0.05	0.05
SR4 Friction parameter	β	°	65.0	67.5
SR4 Friction exponent	n	-	1.6	0.95
SR4 Dilation parameter	φ	°	45.0	66.5
SR4 Dilation exponent	m	-	1.6	0.8
SR4 Deviatoric plane parameter	β_0^π	-	0.6	0.6
Critical state friction angle	φ_{cs}	°	29.5	32.4
SR4 Deviatoric plane parameter 2	β_1^π	-	0.6	0.6
SR4 Deviatoric plane exponent	α^π	-	0.25	0.25
Biot constant	α	-	1.0	1.0

Table A 2

Geomechanical properties for salt lithology.

Property	Symbol	Units	Salt
Grain Stiffness	K_g	MPa	30,000
Grain Density	ρ_g	$\frac{Kg}{m^3}$	2140
Young's modulus	E	MPa	5000
Poisson's ratio	ν	-	0.3
Yield strength	q_y	MPa	0.1
Viscoplastic Constant	K_{visc}	MPa·Ma	0.01
Viscoplastic Exponent	n_{visc}	-	1

Depositional profiles derived from restoration

A geomechanical restoration on the selected seismic section (Fig. 1a) is performed to obtain the sediment depositional profiles for the forward evolutionary model. Only the clastic sediments are explicitly represented in the present-day model for restoration because: 1) salt is expected to be weak relative to the sediments and should not impose a constraint in deformation during restoration and 2) salt is expected to experience large geometrical changes which may lead to numerical instabilities in elastic geomechanical restorations. The length of the basin is extended beyond the seismic section data to the approximate location of the Titan mini-basin centre so that 1) the location of interest is away from the boundary and 2) we consider the appropriate salt flow pathway length towards the diapir in the forward model. Six formations are defined for restoration consistent with interpreted seismic tops which they terminate laterally where they intersect the salt. The restoration considers a flat restoration datum to which the formation tops are backstripped assuming vertical shear with decompaction (Figure A 1). At the end of each restoration a restored formation thickness profile for the top formation is obtained. Then the top formation is removed, and the restoration simulation continues with the back-stripping of the next formation. At the end of the whole restoration 6 restoration thickness profiles are obtained. Those were later idealised to piecewise linear functions using two lines with different slopes to facilitate subsequent calibration (see Figure A 2 a and b). In addition, the thicknesses of each restored formation were divided into several layers for the forward simulation (see Table A 3). The depositional thickness profiles for the two sand layers are arbitrarily defined to represent 4 isolated sand channels, each of which has a depositional thickness of 120 m and an approximate length of 700 m (see Sed_hor_03 and Sed_hor_04 in Figure A 2 c).

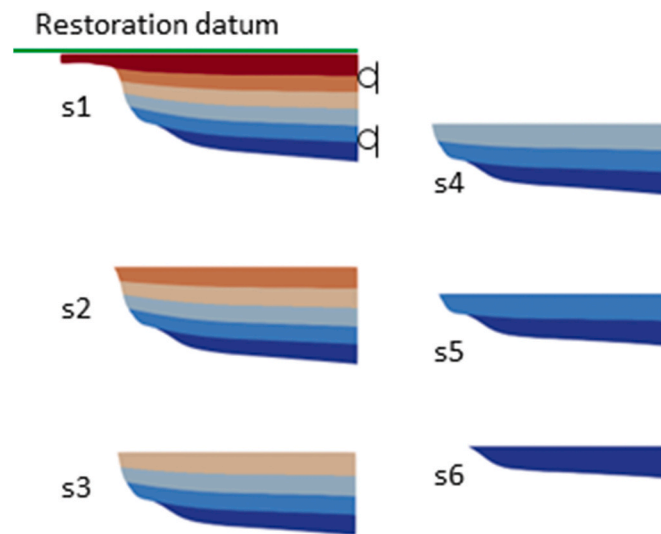


Fig. A 1. Geometries at the end of each of the six restoration stages simulated (s1 to s6). In s1 the boundary conditions for the restoration model are indicated.

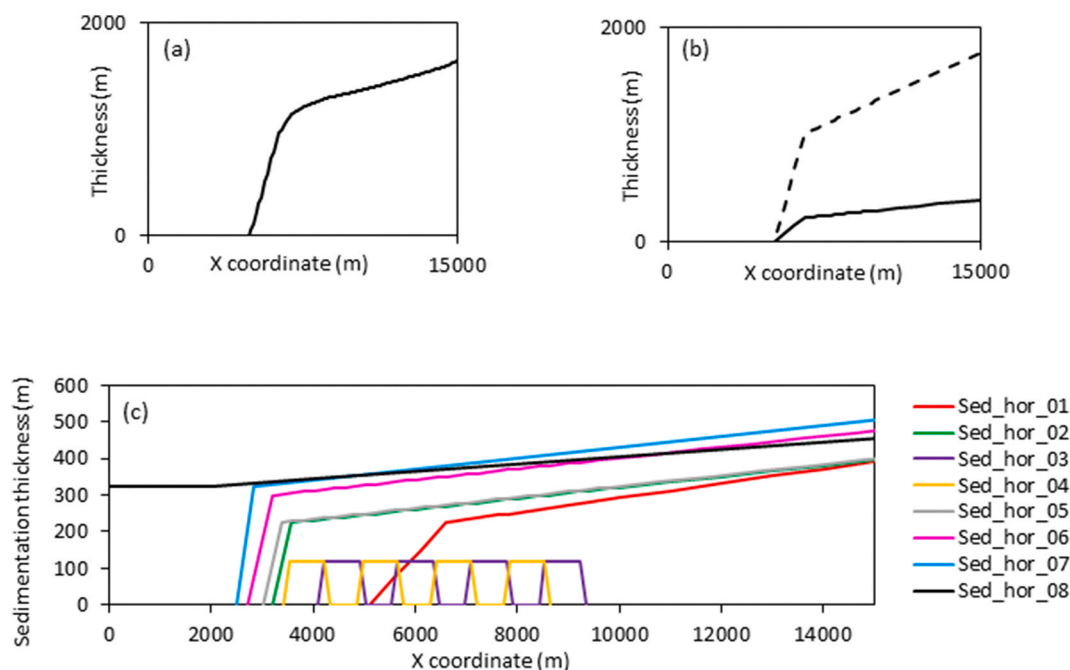


Fig. A 2. (a) Example of a restored formation thickness profile and (b) the same profile idealised to a piece-wise linear function (discontinuous line), with a subsequent formation sub-division in several layers (continuous line). (c) Calibrated sedimentation profiles used to define the depositional thickness at each X coordinate in the forward model. Sed_hor 03 and 04 define isolated sand channels.

Table A 3

Depositional formations considered in the numerical models. Sed_hor indicates the sedimentation horizon profile used for defining the depositional thickness of each layer (see Fig. 9).

Layer name	Lithology	Depositional Thickness Profile	Sedimentation Duration (Ma)	Top Horizon Age (Ma)
Salt	Salt	–	–	5.324
Pliocene01	Mudstone	Sed_hor_01	0.55	4.774
Pliocene02	Mudstone	Sed_hor_01	0.55	4.224
Pliocene03	Mudstone	Sed_hor_01	0.55	3.674
Pliocene04	Mudstone	Sed_hor_01	0.55	3.124
Pliocene05	Mudstone	Sed_hor_02	0.55	2.574
Pleistocene01	Mudstone	Sed_hor_02	0.198	2.376
Pleistocene02	Sand	Sed_hor_03	0.099	2.277
Pleistocene03	Mudstone	Sed_hor_02	0.198	2.079
Pleistocene04	Sand	Sed_hor_04	0.099	1.98
Pleistocene05	Mudstone	Sed_hor_05	0.198	1.782
Pleistocene06	Mudstone	Sed_hor_05	0.198	1.584
Pleistocene07	Mudstone	Sed_hor_06	0.198	1.386
Pleistocene08	Mudstone	Sed_hor_06	0.198	1.188
Pleistocene09	Mudstone	Sed_hor_07	0.198	0.99
Pleistocene10	Mudstone	Sed_hor_07	0.198	0.792
Pleistocene11	Mudstone	Sed_hor_07	0.198	0.594
Pleistocene12	Mudstone	Sed_hor_08	0.198	0.396
Pleistocene13	Mudstone	Sed_hor_08	0.198	0.198
Pleistocene14	Mudstone	Sed_hor_08	0.198	0

References

Albertz, M., Lingrey, S., 2012. Critical state finite element models of contractional fault-related folding: Part 1. Structural analysis. *Tectonophysics* 576–577, 133–149.
 Albertz, M., Sanz, P.F., 2012. Critical state finite element models of contractional fault-related folding: Part 2. Mechanical analysis. *Tectonophysics* 576–577, 150–170.
 Athy, L.F., 1930. Density, porosity, and compaction of sedimentary rocks. *AAPG (Am. Assoc. Pet. Geol.) Bull.* 14 (1), 1–24.
 Azadpoura, M., Shadmanaman, N., Kadkhodaie-Ilkhchi, A., Sedghipour, M.R., 2015. Pore pressure prediction and modeling using well-logging data in one of gas fields in south of Iran. *J. Petrol. Sci. Eng.* 128, 15–23.
 Bahmaei, Z., Hosseini, E., 2020. Pore pressure prediction using seismic velocity modeling: case study, Sefid-Zakhor gas field in Southern Iran. *J. Pet. Explor. Prod. Technol.* 10, 1051–1062.

Bowers, G.L., 1995. Pore Pressure Estimation from Velocity Data: Accounting for Overpressure Mechanisms besides Undercompaction. *SPE Drilling & Completion*, pp. 89–95.
 Bowers, G.L., 2001. Offshore Technology Conference. Determining an Appropriate Pore-Pressure Estimation Strategy, 2001. OnePetro, Houston, Texas, pp. 1–14. April.
 Bowers, G.L., Katsube, T.J., 2002. The role of shale pore structure on the sensitivity of wire-line logs to overpressure. In: Huffman, A.R., Bowers, G.L. (Eds.), *Pressure Regimes in Sedimentary Basins and Their Prediction*. AAPG, pp. 43–60.
 Brahma, J., Sircar, A., Karmakar, G.P., 2013. Pre-drill pore pressure prediction using seismic velocities data on flank and synclinal part of Atharamura anticline in the Eastern Tripura, India. *J. Pet. Explor. Prod. Technol.* 3, 93–103.
 Broichhausen, H., Littke, R., Hantschel, T., 2005. Mudstone compaction and its influence on overpressure generation, elucidated by a 3D case study in the North Sea. *Int. J. Earth Sci.* 94 (5), 956–978.

- Colwart, G., Burton, R.C., Eaton, L.F., Hodge, R.M., Blake, K., 2007. Lessons Learned on Sand-Control Failure and Subsequent Workover at Magnolia Deepwater Development. SPE, pp. 1–17.
- CoreLab, 2003. Petrographic Analysis of Conventional Core Samples from: ConocoPhillips OCS-G 11573, #2 ST-2, Garden Banks 783. Offshore Louisiana.
- Couzens-Schultz, B.A., Azbel, K., 2014. Predicting pore pressure in active fold-thrust systems: an empirical model for the deepwater Sabah foldbelt. *J. Struct. Geol.* (69), 465–480.
- Crook, A.J.L., Willson, S.M., Yu, J.G., Owen, D.R.J., 2006. Predictive modelling of structure evolution in sandbox experiments. *J. Struct. Geol.* 28 (5), 729–744.
- Crook, A.J.L., Obradors-Prats, J., Somer, D., Peric, D., Lovely, P., Kaciewicz, M., 2018. Towards an integrated restoration/forward geomechanical modelling workflow for basin evolution prediction. *Oil & Gas Science and Technology - Rev. IFP Energies Nouvelles* 73, 1–19.
- Dickinson, G., 1953. Geological aspects of abnormal reservoir pressures in Gulf Coast Louisiana. AAPG (Am. Assoc. Pet. Geol.) Bull. 37 (2), 410–432.
- Dugan, B., Flemings, B., 2000. Overpressure and fluid flow in the New Jersey continental slope: implications for slope failure and cold seeps. *Science* 289, 288–291.
- Eaton, B.A., 1975. The equation for geopressure prediction from well logs. SPE 1–11.
- Eaton, L.F., Actis, S.C., Williamson, R.N., 2005. Deepwater batchset operations through the Magnolia shallow water flow sand. SPE 1–20.
- Ewy, R., Drirkzwager, J., Bovberg, C., 2020. Claystone porosity and mechanical behavior vs. geologic burial stress. *Mar. Petrol. Geol.* 121, 1–20.
- Flemings, P.B., Lupa, J.A., 2004. Pressure prediction in the bullwinkle basin through petrophysics and flow modeling (green canyon 65, Gulf of Mexico). *Mar. Petrol. Geol.* 21 (10), 1311–1322.
- Gouly, N.R., Sargent, C., 2016. Compaction of diagenetically altered mudstones - Part 2: implications for pore pressure estimation. *Mar. Petrol. Geol.* 77, 806–818.
- Hansen, S., 1996. A compaction trend for Cretaceous and Tertiary shales on the Norwegian Shelf based on sonic transit times. *Petrol. Geosci.* 2, 159–166.
- Hantschel, T., Kauerauf, A.I., 2009. Fundamentals of Basin and Petroleum Systems Modeling. Springer, Aachen, Germany.
- Hart, B.S., Flemings, P.B., Deshpande, A., 1995. Porosity and pressure: role of compaction disequilibrium in the development of geopressures in a Gulf Coast Pleistocene basin. AAPG (Am. Assoc. Pet. Geol.) Bull. 23, 45–48.
- Heaton, L., Petmecky, S., Kirkland, B., 2020. Modelling the Impact of Geological Uncertainty on Lateral Fluid Transfer and Pore Pressure in Overpressured Basins. Paper presented at the Third EAGE Workshop on Pore Pressure Prediction.
- Heidari, M., Nikolinakou, M.A., Hudec, M.R., Flemings, P.B., 2016. Geomechanical analysis of a welding salt layer and its effects on adjacent sediments. *Tectonophysics* 683, 172–181.
- Heidari, M., Nikolinakou, M.A., Hudec, M.R., Flemings, P.B., 2021. Impacts of vertical salt welding on pore pressure, stresses, and deformation near the weld. *Mar. Petrol. Geol.* 133 (105259), 1–18.
- Herschel, W.H., Bulkeley, R., 1926. Konsistenzmessungen von Gummi-benzollösungen. *Kolloid Z.* 39, 291–300. <https://doi.org/10.1007/BF01432034>.
- Hubbert, M.K., Rubey, W.W., 1959. Role of fluid pressure in mechanisms of overthrust faulting. AAPG (Am. Assoc. Pet. Geol.) Bull. 70, 167–206.
- Issler, D.R., 1992. A new approach to shale compaction and the stratigraphic restoration, Beaufort-Mackenzie Basin and Mackenzie Corridor, Northern Canada. AAPG (Am. Assoc. Pet. Geol.) Bull. 76 (8), 1170–1189.
- Kane, I.A., McGee, D.T., Jobe, Z.R., 2012. Halokinetic effects on submarine channel equilibrium profiles and implications for facies architecture: conceptual model illustrated with a case study from Magnolia Field. In: Alsop, G.I., Archer, S.G., Hartley, A.J., Grant, N.T., Hodkinson, R. (Eds.), *Salt Tectonics, Sediments and Prospectively*, pp. 289–302. London.
- Lahann, R.W., Swarbrick, R.E., 2011. Overpressure generation by load transfer following shale framework weakening due to smectite diagenesis. *Geofluids* 11, 362–375.
- Lewis, R.W., Schrefler, B.A., 1998. *The Finite Element Method in the Static and Dynamic Deformation and Consolidation of Porous Media*, second ed. John Wiley & Sons, Inc, Chichester.
- Li, C., Zhang, L., Luo, X., Lei, Y., Yu, L., Cheng, M., Wang, Z., 2021. Overpressure generation by disequilibrium compaction or hydrocarbon generation in the Paleocene Shahejie Formation in the Chechen Depression: insights from logging responses and basin modelling. *Mar. Petrol. Geol.* 133 (105258), 1–15.
- Liu, H., Wang, Y., Jiang, Y., Yuan, F., Chen, K., Guo, Z., 2019. Quantification models of overpressuring in paleogene source rocks of the raoyang depression, bohai bay basin, China. *Mar. Petrol. Geol.* 109, 607–622.
- Lopez, J.L., Rappold, P.M., Ugueto, G.A., Wieseneck, J.B., Vu, C.K., 2004. Integrated shared earth model: 3D pore-pressure prediction and uncertainty analysis. *Lead. Edge* 23, 52–59.
- Lovely, P., Kaciewicz, M., Crook, A.J.L., Obradors-Prats, J., 2018. Fully Coupled Poro-Mechanical Basin Models for Pressure and Effective Stress Prediction, with Application to a Mini-Basin in Voluminous Salt. SEG, pp. 321–325.
- Luo, X., Vasseur, G., 1992. Contributions of compaction and aquathermal pressuring to geopressure and the influence of environmental conditions. AAPG (Am. Assoc. Pet. Geol.) Bull. 76, 1550–1559.
- Luo, X., Wang, Z., Zhang, L., Yang, W., Liu, L., 2007. Overpressure generation and evolution in a compressional tectonic setting, the southern margin of Junggar Basin, northwestern China. AAPG (Am. Assoc. Pet. Geol.) Bull. 91 (8), 1123–1139.
- Luo, G., Hudec, M.R., Flemings, P.B., Nikolinakou, M.A., 2017. Deformation, stress and pore pressure in an evolving suprasalt basin. *J. Geophys. Res. Solid Earth* 122 (7), 5663–5690.
- Neumaier, M., Littke, R., Hantschel, T., Maerten, L., Joonnekindt, J.P., Kukla, P., 2014. Integrated charge and seal assessment in the Monagas fold and thrust belt of Venezuela. AAPG (Am. Assoc. Pet. Geol.) Bull. 98 (7), 1325–1350.
- Nguyen, B.T.T., Kido, M., Okawa, N., Fu, H., Kazizaki, S., Imahori, S., 2016. Compaction of smectite-rich mudstone and its influence on pore pressure in the deepwater Joetsu Basin, Sea of Japan. *Mar. Petrol. Geol.* 78, 848–869.
- Nikolinakou, M.A., Flemings, P.B., Hudec, M.R., 2014. Modeling stress evolution around a rising salt diapir. *Mar. Petrol. Geol.* 51, 230–238.
- Nikolinakou, M.A., Flemings, P.B., Heidari, M., Hudec, M.R., 2018. Stress and pore pressure in mudrocks bounding salt systems. *Rock Mech. Rock Eng.* 51, 3883–3894.
- Obradors-Prats, J., Rouainia, M., Aplin, A.C., Crook, A.J.L., 2016. Stress and pore pressure in complex tectonic settings predicted with coupled, 3D geomechanical-fluid flow models. *Mar. Petrol. Geol.* 76, 464–477.
- Obradors-Prats, J., Rouainia, M., Aplin, A.C., Crook, A.J.L., 2017a. Assessing the implications of tectonic compaction on pore pressure using a coupled geomechanical approach. *Mar. Petrol. Geol.* 79, 31–43.
- Obradors-Prats, J., Rouainia, M., Aplin, A.C., Crook, A.J.L., 2017b. Hydromechanical modeling of stress, pore pressure, and porosity evolution in fold-and-thrust belt systems. *J. Geophys. Res. Solid Earth* 122 (11), 9383–9403.
- Obradors-Prats, J., Rouainia, M., Aplin, A.C., Crook, A.J.L., 2019. A diagenesis model for geomechanical simulations: formulation and implications for pore pressure and development of geological structures. *J. Geophys. Res. Solid Earth* 124 (5), 4452–4472.
- Osborne, M.J., Swarbrick, R.E., 1997. Mechanisms for generating overpressure in sedimentary basins: a reevaluation. AAPG (Am. Assoc. Pet. Geol.) Bull. 81, 1023–1041.
- Ostermeier, R.M., Pelletier, J.H., Winter, C.D., Nicholson, J.W., Rambow, F.H., Cowan, K.M., 2000. Dealing with shallow-water flow in the deepwater Gulf of Mexico. SPE 1–12.
- Ostermeier, R.M., Pelletier, J.H., Winter, C.D., Nicholson, J.W., 2001. Trends in Shallow Sediment Pore Pressures-Deepwater Gulf of Mexico. SPE, pp. 1–12.
- Procyk, A.D., Jamieson, D.P., Miller, J.A., Burton, R.C., Hodge, R.M., Morita, N., 2007. Completion Design for a Highly Compacting Deepwater Field, Proceedings of the SPE Annual Technical Conference and Exhibition, 2007. Society of Petroleum Engineers, Anaheim, California, U.S.A., pp. 1–21. November.
- Raymer, L.L., Hunt, E.R., Gardner, J.S., 1980. An Improved Sonic Transit Time-To-Porosity Transform, *SPWLA Twenty-First Annual Logging Symposium*, Lafayette. OnePetro, Louisiana, pp. 1–13, 8th-11th July 1980.
- Roberts, D.T., Crook, A.J.L., Profit, M.L., Cartwright, J.A., 2015. Investigating the Evolution of Polygonal Fault Systems Using Geomechanical Forward Modeling. US Rock Mechanics/Geomechanics Symposium, San Francisco, CA, USA. Paper presented at the 49th.
- Ruh, J.B., 2017. Effect of fluid pressure distribution on the structural evolution of accretionary wedges. *Terra. Nova* 29, 202–210.
- Saffer, D.M., Tobin, H.J., 2011. Hydrogeology and mechanics of subduction zone forearc fluid flow and pore pressure. *Annu. Rev. Earth Planet Sci.* 39, 157–186.
- Sathar, S., Jones, S., 2016. Fluid overpressure as a control on sandstone reservoir quality in a mechanical compaction dominated setting: Magnolia Field, Gulf of Mexico. *Terra. Nova* 28 (3), 155–162.
- Sayers, C.M., Johnson, G.M., Denyer, G., 2002. Predrill pore-pressure prediction using seismic data. *Geophysics* 67 (4), 1020–1326.
- Schlumberger, 1989. *Log Interpretation Principles/applications*. Schlumberger Educational Services, Houston, Texas.
- Smart, K.J., Ferrill, D.A., Morris, A.P., McGinnis, R.N., 2012. Geomechanical Modeling of Stress and Strain Evolution during Contractional Fault-Related Folding. *Tectonophysics*, pp. 171–196.
- Stomp, R.J., Fraser, G.J., Actis, S.C., Eaton, L.F., Freedman, K.C., 2004. Deepwater DST planning and operations from a DP Vessel. SPE 1–19.
- Swarbrick, R.E., 2012. Review of pore-pressure prediction challenges in high-temperatures areas. *Lead. Edge* 31, 1288–1294.
- Thornton, D.A., Crook, A.J.L., 2014. Predictive modelling of the evolution of fault structure: 3-D modelling and coupled geomechanical/flow simulation. *Rock Mech. Rock Eng.* 47 (5), 1533–1549.
- Tingay, M.R.P., Hillis, R.R., Swarbrick, R.E., Morley, C.K., Damit, A.R., 2009. Origin of overpressure and pore-pressure prediction in the Baram province, Brunei. AAPG (Am. Assoc. Pet. Geol.) Bull. 93, 51–74.
- Vidal-Royo, O., Hardy, S., Muñoz, J.A., 2011. The roles of complex mechanical stratigraphy and syn-kinematic sedimentation in fold development: insights from discrete-element modelling and application to the Pico del Aguila anticline (External Sierras, Southern Pyrenees). In: *Kinematic Evolution and Structural Styles of Fold-And-Thrust Belts*, 349. Geological Society, London, Special Publications, pp. 45–60.
- Weissenburger, K.S., Borbas, T., 2004. Fluid properties, phase and compartmentalization: Magnolia Field case study, deepwater Gulf of Mexico, USA. *Geological Society* 237, 231–255.
- Wood, D.M., 1990. *Soil Behaviour and Critical State Soil Mechanics*. Cambridge University Press.
- Wyllie, M.R.J., Gregory, A.R., Gardner, L.W., 1956. Elastic wave velocities in heterogeneous and porous media. *Geophysics* 21, 41–70.
- Yardley, G.S., Swarbrick, R.E., 2000. Lateral transfer: a source of additional overpressure? *Mar. Petrol. Geol.* 17 (4), 523–537.
- Zhang, J., 2011. Pore pressure prediction from well logs: methods, modifications, and new approaches. *Earth Sci. Rev.* 108 (1–2), 50–63.
- Zong, J.C., Coskun, S., Stewart, R.R., Dyaun, N., Myers, M.T., 2015. Salt densities and velocities with application to Gulf of Mexico salt domes, Salt Challenges in Hydrocarbon Exploration SEG Annual Meeting Post-Convention Workshop 1–5. New Orleans.